



Research paper

Heat transfer investigations on a thermally superior alternative for the flux switching permanent magnet electric motor

Tohid Sharifi ^{a,*}, Alireza Eikani ^b^a Department of Electrical Engineering, Electrical Machines and Transformers Research Laboratory (EMTRL), Amirkabir University of Technology (Tehran Polytechnic), Tehran, Iran^b Advanced Motion Systems Research Lab, School of Electrical and Computer Engineering, College of Engineering, University of Tehran, Tehran, Iran

ARTICLE INFO

Keywords:
 Heat transfer
 Permanent magnet motors
 Heat flow diagram
 Heat generation
 Electromagnetic torque
 Thermal experiment

ABSTRACT

Severe temperature rise is not tolerated in the windings and permanent magnets (PMs) of the electric motors due to the resultant performance degradation, increased maintenance cost, and eventually the short-circuit faults. This article suggests a new approach to mitigating the temperature of components in a flux-switching PM (FSPM) motor using the concepts of heat transfer paths and heat flow diagrams. Accordingly, changing the location of the armature windings from the adjacency of the PMs to the middle tooth of the E-core stator blocks brings multiple thermal and electromagnetic merits to the proposed motor. In the heat generation stage, the numerical studies indicate that the total power losses of the motor decrease from 56.6 W to 39.6 W. Moreover, the maximum working temperature of the windings and PMs is cut by 36.4% and 40%, respectively, demonstrating the remarkable effect of the proposed strategy on temperature. From the electromagnetic point of view, the proposed motor outperforms the E-core FSPM motor due to the separation of the electrical and magnetic loading sources, resulting in the uniformity of the steel cores' flux density. Lastly, the thermal and electromagnetic experimental studies are provided to verify the outcomes of the analytical and numerical investigations.

1. Introduction

Sustainable power delivery in a limited space has become an irreplaceable necessity for industrial applications and domestic appliances [1,2]. Considering the recent prominent progress in manufacturing technologies and material advancements, PM electric motors can provide a stable electromagnetic torque under the volume/weight constraints, provided that the high-density electrical and magnetic loadings simultaneously play roles in the energy conversion [3–5]. Escalations in the electrical loadings of the armature windings go together with the high copper loss densities, which exacerbates the thermal stress in the hotspots. Because of the heat transfer paths from the hotspots to the PMs, the intensifications in the temperature of the magnetic loading sources are accompanied by partial demagnetization, potentially causing a serious decline in the delivered electromagnetic torque of the motor [6,7]. On more serious occasions, the severe temperature rise damages the insulations of the armature windings and creates a dangerous ground for the short-circuit faults, which results in considerable shortenings in the lifetime of the PM electric motors [8,9]. Incorporating thermal studies in the design of electromagnetic systems can avoid performance deteriora-

tion by providing effective temperature mitigation strategies. Generally, in the state-of-the-art studies, two approaches are put forward to confront the challenge of temperature rise in electric motors [10].

In the first category, a straightforward method is practically utilized when the hotspots are exposed to the cooling circuits directly or indirectly, for which several coolants can serve, including air, water, or oil. Cooling jackets are structures that carry liquid coolants across different motor regions and accomplish forced convection [11,12]. Although installing the water jackets inside the motor casing, equipped with annular fins on the inner surface, has brought sufficient cooling effects to maintain the temperature of the PMs below 92 °C [13], it is indicated that implementing them on the outer surface of the stator core (closer to the hotspots) has granted much more benefits for temperature mitigation [14]. Besides the convection, which is improved by the forced cooling mechanisms, the conduction heat transfer can be improved using potting materials such as silicon gelatin with a thermal conductivity of $2 \text{ W.m}^{-1}\text{.}^{\circ}\text{C}^{-1}$, which as indicated in [15], 17 °C more temperature reduction has been achieved in a PMSM motor. Due to their flexibility and thermal conductivity of approximately $2000 \text{ W.m}^{-1}\text{.}^{\circ}\text{C}^{-1}$ [16–18] (much more than the potting materials), the heat pipes are also com-

* Corresponding author.

E-mail addresses: tohidsharifi@aut.ac.ir (T. Sharifi), alirezaeikani@gmail.com (A. Eikani).

Nomenclature

Abbreviations and acronyms

Back-EMF	Back electromotive force
BLAC	Brushless AC
CFD	Computational fluid dynamics
FE	Finite element
FSPM	Flux switching permanent magnet
HTC	Heat transfer coefficient
KCL	Kirchhoff's current law
MRL	Manufacturing readiness level
MT	Middle teeth of the E-core stator blocks
PM	Permanent magnet
PMSM	Permanent magnet synchronous motor
PMT	Stator teeth adjacent to the permanent magnets
RTD	Resistance temperature detector
TRL	Technological readiness level

Greek symbols

δ	Airgap length	m
λ	Thermal conductivity of materials	$W.m^{-1}.^{\circ}C^{-1}$
$\lambda_{eq,Airgap}$	Equivalent thermal conductivity of airgap fluid.....	$W.m^{-1}.^{\circ}C^{-1}$
λ_{eq}	Equivalent thermal conductivity	$W.m^{-1}.^{\circ}C^{-1}$
λ_i	Thermal conductivity of the component i ..	$W.m^{-1}.^{\circ}C^{-1}$
λ_x	Thermal conductivity of the component in the x direction.....	$W.m^{-1}.^{\circ}C^{-1}$
λ_y	Thermal conductivity of the component in the y direction.....	$W.m^{-1}.^{\circ}C^{-1}$
λ_z	Thermal conductivity of the component in the z direction.....	$W.m^{-1}.^{\circ}C^{-1}$
ω	The rotational speed of the motor	$rad.s^{-1}$
ρ	Density of materials	$kg.m^{-3}$
ρ_{cu}	Density of copper.....	$kg.m^{-3}$
ρ_{eq}	Equivalent density	$kg.m^{-3}$
σ_{PM}	Permanent magnet conductance	Ω^{-1}

Mathematical symbols

A_{con}	The surface area of the conductors in the windings...	m^2
B_m	Maximum flux density	T
C_i	Thermal capacitance of the component i.....	$J.^{\circ}C^{-1}$
$C_{p,eq}$	Equivalent specific heat capacity	$J.kg^{-1}.^{\circ}C^{-1}$
C_p	Specific heat capacity of materials	$J.kg^{-1}.^{\circ}C^{-1}$
C_p	Thermal capacitance of the PM	$J.^{\circ}C^{-1}$
D_w	Diameter of the conductors in the windings	m
f	frequency	Hz
I_{rms}	Root mean square of the armature current.....	A

bined with the forced convection methods, for which the location of installation is determined from a trade-off between the electromagnetic and thermal objectives, and can be as highly effective as $30\text{ }^{\circ}\text{C}$ in the temperature reduction [19,20]. The same mechanism is the case for the phase change materials, while their effect is not as significant as the potting materials and heat pipes [21]. Creating a direct contact surface between the coolant and hotspot is the most effective and efficient way of alleviating the thermal stress of the motor [22]. In [23], the massive reduction of the hotspot temperature from $283\text{ }^{\circ}\text{C}$ to $135\text{ }^{\circ}\text{C}$ (more than 50%), which brings a sustainable, faultless performance for the radial cup-winding PMSM in the structure of a flywheel energy storage system, demonstrated the competence of the direct cooling. The convective HTC, compactness, and energy efficiency can be improved further by implementing direct oil spray cooling using spiral, full-cone, or half-cone nozzles [24,25]. The CFD analysis on the shaft-sprayed coolant

J_v	Harmonic eddy current amplitude.....	A
k_{eddy}	Coefficient of the eddy-current loss of the core	$W.Hz^{-2}.T^{-2}$
k_{exc}	Coefficient of the excess loss of the core	$W.Hz^{-1.5}.T^{-1.5}$
k_{hyst}	Coefficient of the hysteresis loss of the core	$W.Hz^{-1}.T^{-\alpha}$
L_{acw}	Length of the active part of the coil	m
L_{enw}	Length of the end part of the coil.....	m
L_i	Length of the component i	m
M_i	Mass of the component i	kg
N	Number of turns in the coils of winding	
P	Total power losses	W
P_{ac}	AC component of the copper losses.....	W
P_{core}	Core losses	W
$P_{cu,acw}$	Copper losses in the active part of the windings	W
$P_{cu,enw}$	Copper losses in the end part of the winding	W
P_{cu}	Copper losses	W
P_{dc}	DC component of the copper losses	W
P_{eddy}	Eddy current losses of the PMs	W
$Q_{acw,mto}$	The heat flow from the active winding to the middle tooth.....	W
$Q_{acw,to}$	The heat flow from the active winding to the stator tooth.....	W
Q_c	The charging heat of the PM	W
$Q_{enw,mto}$	The heat flow from the end winding to the middle tooth.....	W
$Q_{enw,PM}$	The heat flow from the end winding to the PM.....	W
$Q_{m,ag}$	The heat flow from the middle tooth to the airgap in the E-core FSPM motor	W
$Q_{m,amb}$	The heat flow from the middle tooth to the ambient in the proposed motor	W
$Q_{mto,ag}$	The heat flow from the middle tooth to the airgap in the proposed motor	W
$Q_{PM,to}$	The heat flow from the PM to the stator tooth in the E-core FSPM motor	W
$Q_{to,ag}$	The heat flow from the stator tooth to the airgap	W
$Q_{yo,amb}$	The heat flow from the stator yoke to the ambient....	W
R	Total thermal resistance of the coil	Ω
R_{acw}	Electrical resistance of the active part of the winding..	Ω
R_{enw}	Electrical resistance of the end part of the winding....	Ω
R_{is}	Inner radius of the stator	m
r_{os}	Outer radius of the rotor	m
Re	Reynolds number	
T	Temperature of motor components.....	$^{\circ}\text{C}$
T_{PM}	PM temperature	$^{\circ}\text{C}$
v	Kinematic viscosity of the airgap fluid.....	$m^2.s^{-1}$
V_{PM}	Permanent magnet volume	m^3

to the hotspots has demonstrated that the HTC under the nominal and maximum rotational speeds reaches values of $3457.9\text{ }W.m^{-2}.^{\circ}\text{C}^{-1}$ and $13581.5\text{ }W.m^{-2}.^{\circ}\text{C}^{-1}$, respectively [26].

Aside from the cooling system design, which is founded on the TRL and MRL [27,28], the advancements in the material properties can be explored and exploited, where the material of the motor components can be replaced by their thermally efficient alternatives to bring much more comfort from the thermal perspective [29,30]. Although these methods can be used with the forced convection cooling methods in a hybrid package, they can be implemented exclusively to bring temperature uniformity, mitigation, and minimize maintenance efforts [31]. In [32], the insulations of the conductors inside the slots are replaced by materials with a higher thermal conductivity, for which polyamide-imide/boron nitride composites are implemented in the experimental setup. Without a particular cooling system (under natural convection),

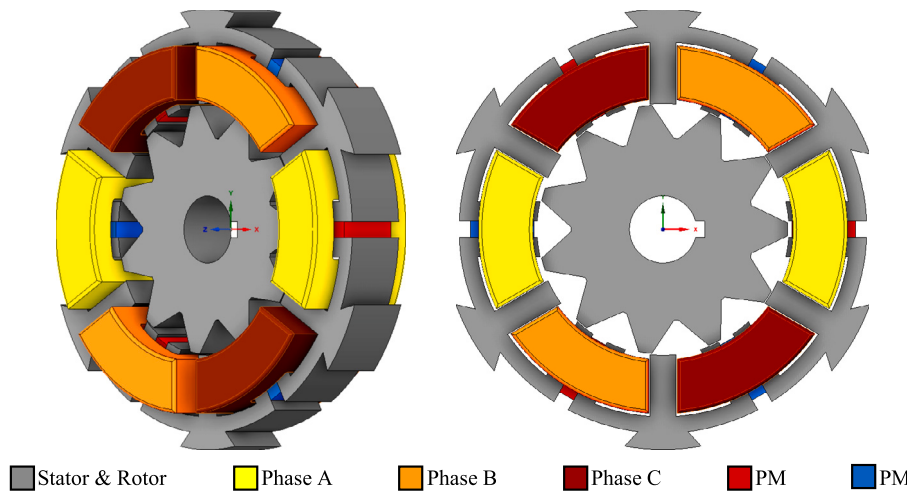


Fig. 1. Three-dimensional (left) and two-dimensional (right) views of the E-core FSPM motor. The red and blue colors of the PMs are utilized to show the anticlockwise and clockwise directions of the magnetic flux.

although the effectiveness on the winding's temperature level is less than 8°C when using insulations with the thermal conductivity of $7.6 \text{ W.m}^{-1.\text{C}}^{-1}$ rather than $0.1 \text{ W.m}^{-1.\text{C}}^{-1}$, the temperature uniformity of the slots has been improved significantly, relieving the hotspots. Replacing the NdFeB magnets with SmCo pieces is the strategy of [33] to increase the temperature rise tolerance of the PMSM in the structure of a 0.5 kWh flywheel energy storage system, where the complete thermal isolation is available between the rotor and stator sides due to the vacuum conditions inside the motor. With this change, there is no need to implement forced cooling topologies on the rotor side. However, this method cannot alleviate the temperature and, therefore, cannot help the performance degradation due to partial demagnetization [34].

Lack of knowledge: In the design of cooling systems (first category), multiple criteria should be investigated besides thermal effectiveness, including maintenance, manufacturing and material costs, compactness, stray losses, and safety [35]. The water jacket strategy requires periodic maintenance to employ the sealants and centrifugal pumps properly [36]. In the direct methods, due to the contact between the coolant and heat sources, safety considerations should be included in the form of adding electrically insulating materials such as impregnating resin Voltatex 4200 in the region [37]. All of the mentioned methods require manufacturing costs to prepare the cooling structures, while the cost of materials in the hybrid structures (with potting materials, phase change materials, or the heat pipes) reaches its highest portion. Moreover, due to the stray losses in the components of the cooling systems, the efficiency of the electric motors would deteriorate [38]. Although these issues are solved to much extent in the temperature rise tolerance strategy, their effectiveness in the cooling is not comparable and reliable, and therefore, they should be utilized in the hybrid structures with the first category's systems, causing their advantages to be disappeared. Moreover, the TRL or MRL may not be sufficient to implement these methods, particularly in the case of advanced materials [39].

Contributions of this study: In this study, a new approach is developed to mitigate the temperature of hotspots and PMs in the structure of an E-core FSPM motor. The basic concepts of heat transfer in the form of heat flow diagrams are utilized to convert this motor to a thermally superior alternative with much more prominent performance in the heat generation and heat transfer stages. The presented approach has the capability to significantly influence the temperature of the PMs and armature windings, while there are no additional cooling structures and components, maintenance efforts, safety considerations, and stray losses in this approach to achieve this target. Therefore, besides the fact that the approach combines the advantages of the first and second strategies, the electromagnetic performance of the motor will be affected in a positive way due to the power loss reduction and the resultant uniform flux

density distribution, which are evident in the efficiency and electromagnetic torque capabilities of the motor. The numerical investigations for the thermal performance of the E-core FSPM and proposed motors have approved the results of the heat flow diagrams, which are verified by the experimental test results. Additionally, electromagnetic test results are provided to ensure the BLAC operation and torque performance of the proposed motor.

Organization: The rest of this study is organized as follows. In section 2, the heat transfer aspects of the E-core FSPM and its inherent thermal disadvantages are explained using the heat flow diagram. Subsequently, in section 3, the heat transfer paths of this motor are modified and improved from the hotspots to the surrounding ambient, creating a base for the proposed motor. The heat generation and heat transfer capabilities of both motors are investigated numerically in section 4 to calculate the extension and direction of changes in the power losses and the component's temperature values. Then, in section 5, the motor is manufactured, and the experimental thermal analyses verify the results of the numerical studies. To ensure the electromagnetic performance of the motor, section 6 provides a detailed explanation about the operation principles of the proposed motor and compares its electromagnetic performance with the E-core FSPM motor. The results of the numerical electromagnetic study will also be verified with experimental tests on the manufactured motor. Finally, in section 7, the main conclusions of this study are reported.

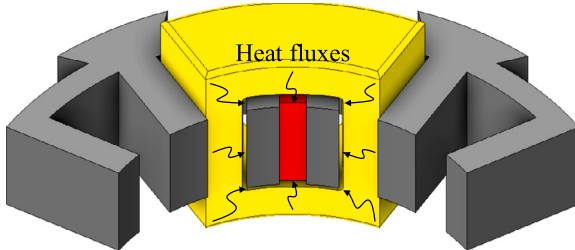
2. Heat transfer aspects of the E-core FSPM motor

As demonstrated in Fig. 1, in the three-phase E-core FSPM motor, the PMs are sandwiched between two adjacent teeth (hereafter called PMTs) of the E-shape core segments, and their combination is surrounded by the armature windings [40]. Therefore, the location of electrical loading sources (armature windings) and magnetic loading sources (PMs) are very close to each other, which would have electromagnetic and thermal consequences. From the electromagnetic viewpoint, this adjacency will cause severe saturating regions in the core, which will provoke the core losses [41]. The electromagnetic characteristics of the E-core FSPM motor are mentioned in Table 1. Here, despite being a low-power, low-speed motor, the current density of the motor is significant, and it can be disclosed that the weight of electrical loading is higher than the magnetic loading. Therefore, from a thermal perspective, as the major portion of the power losses emerges from the electrical loading sources, the hotspots will appear in the armature windings rather than the core or PMs. Considering each coil of the three-phase winding as Fig. 2, the portion inside the slot contributes to the electromagnetic performance,

Table 1

Electromagnetic specifications of the three-phase E-core FSPM motor.

Parameter	Value	Parameter	Value
Rated power (W)	150	Slot fill factor	0.6
Rated current (A)	6	Slot depth (mm)	18
Rated speed (r.p.m.)	1000	Split ratio	0.62
Stator pole number	6	PMT/MT width (mm)	6.065/8
Rotor pole number	11	Airgap length (mm)	0.38
Stator outer diameter (mm)	124.5	Turns per coil	100
Axial length (mm)	20	PM dimensions (mm ²)	5 × 5

**Fig. 2.** Heat transfer paths from the active and end portion of the winding for the E-core FSPM motor.

while the end section of the winding is only responsible for connecting the active portions and does not serve any electromagnetic purpose. Despite being inactive electromagnetically, the generated heat in the end portion of the winding directly affects the temperature of the PMs (Fig. 2), and it can be revealed that almost the entire of the accumulated heat in the end windings finds its way to the ambient through the PMs. For the active portions, because of the adjacency to the PMTs and yoke, the major part of the generated heat is transferred to the stator core through the slot liners and finds its way to the surrounding ambient by passing the motor casing. Moreover, a trivial part is transferred to the rotor through airgap.

2.1. Heat flow diagram of the E-core FSPM motor

It is evident that, under the mentioned slot fill factor (the portion of the slot which is filled by the conductors) of the winding in Table 1, the windings are located close to the PMTs, while there is a significant amount of air and insulations between the windings and middle tooth (hereafter is called MT) of the E-shape stator blocks. Comparing the thermal conductivity of air and stator steel (M350-50A in Table 2), the heat transfer from the windings to the MT is approximately zero. Therefore, as there is no direct thermal connection between the hotspot and the MT, the most thermally-relieved part of the stator core is the MT. These analyses can be reflected in the heat flow diagram of Fig. 3, where only one-sixth of the motor is considered due to the electromagnetic and thermal periodicity in the circumferential direction. The heat generation and heat transfer are modeled using power losses and thermal resistances in the heat flow diagram, respectively. As the objective is to investigate the heat transfer paths from the hotspots to the PMs, only the power losses of the winding (copper losses) are considered. Besides, to study the temperature rise of the PMs, only their specific heat capacities are accounted for in this diagram. In the heat flow diagram, two nodes are considered for the active winding sections (T_{acw} , specified with orange color), located on both sides of the PMT. Another two nodes are used to model the front and back portions of the end windings (T_{enw} , specified with red color.) Full details about the location of the nodes are available in the section view of Fig. 3(a).

After discretization of the E-core FSPM motor segment as Fig. 3(a), the heat flow diagram can be extracted as Fig. 3(b). Considering the similarities between the electrical and thermal equivalent circuits and applying KCL to the blue loop, (1) describes the charging heat flow of

the PM. The purpose of this heat flow is to store some portion of the generated heat of the active ($2Q_{acw,to}$) and end ($2Q_{enw,to}$) sections of the winding in the PMs, while the remainder is transferred through the casing to the ambient ($2Q_{yo,amb}$), and through the airgap to the rotor side ($2Q_{to,ag} + 2Q_{m,ag}$).

$$Q_c = 2Q_{acw,to} + 2Q_{enw,PM} - 2Q_{yo,amb} - 2Q_{to,ag} - 2Q_{m,ag} \quad (1)$$

Due to the insignificance of the thermal conductivity of the circulating air in the airgap compared to that of the stator core, the last two terms of (1) can be neglected, and therefore, the charging heat flow of the PM is achieved as (2). It can be concluded that all of the generated heat in the end winding section is discharged on the PM (end term of (2)), while for the generated heat of the active section (active term of (2)), some portion is released to the ambient. Besides, both terms are applied with a coefficient of two, exacerbating the thermal situation of the PM, and consequently, the massive heat flow in the PM would increase its temperature significantly. Assuming a time interval as t_1 , the temperature of PM can be related to the stored heat as (3), in which, as indicated, increasing the stored heat at each partial time interval leads to the PM temperature escalation.

$$Q_c = \underbrace{2(Q_{acw,to} - Q_{yo,amb})}_{\text{active term}} + \underbrace{2Q_{enw,to}}_{\text{end term}} \quad (2)$$

$$\begin{aligned} T_{PM} &= \int_0^{t_1} \frac{1}{C_p} Q_c(t) dt \\ &= \frac{1}{C_p} \left[2 \int_0^{t_1} Q_{acw,to}(t) dt + 2 \int_0^{t_1} Q_{enw,to}(t) dt - 2 \int_0^{t_1} Q_{yo,amb}(t) dt \right] \end{aligned} \quad (3)$$

3. Proposed thermally-efficient motor

The most problematic thermal feature of the E-core FSPM arises from the fact that all of the generated heat inside the end section of the winding is discharged in the PM as (2), while for the active portion term, there is a relieving way as casing and ambient ($Q_{yo,amb}$). Therefore, to mitigate the temperature of the PM, the location of the end windings should be changed, which leads to improvements in the heat transfer from them to the casing and ambient. In this study, the topology of the E-core FSPM motor of Fig. 1 is changed to the proposed topology of Fig. 4, in which, unlike the FSPM, the MT is surrounded by the armature windings. Despite the fact that in the E-core FSPM motor, the PMs and PMTs are surrounded by the armature windings (hotspots), and there is a direct heat flow path between them, in the proposed structure, as indicated in Fig. 5, the heat fluxes of the end and active portions of the winding is released on the MT, and there is no direct thermal link between the hotspots and PM. Therefore, the major portion of the generated heat in the hotspot is released into the casing and ambient, while the remainder is transferred to the PMT and PM.

3.1. Heat flow diagram of the proposed motor

Unlike the armature winding configuration, the electromagnetic and geometrical specifications of the proposed motor are entirely similar to the E-core FSPM motor, which is indicated in Table 1. Utilizing the electromagnetic and thermal symmetry in the proposed motor, the basic section is shown in Fig. 6(a). Due to the mentioned slot fill factor, there is a substantial volume of air between the active portion of the winding and PMTs, and it can be concluded that there is a relatively substantial thermal resistance between them. However, the matter is not the case between the winding and MT, where the generated heat will be transferred through slot liners from the former to the latter. The mentioned geometrical discretization of Fig. 6(a) can be used to implement the heat flow diagram of the proposed motor as Fig. 6(b).

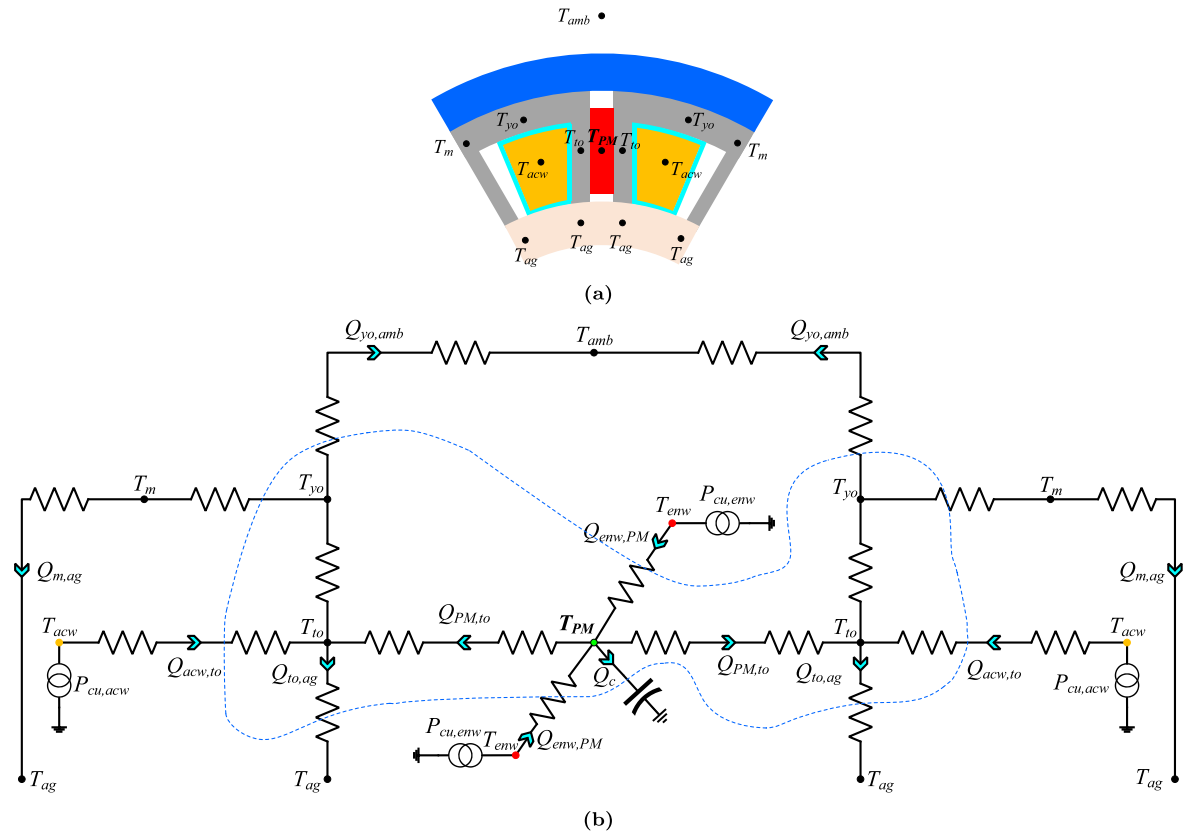


Fig. 3. a) Discretization of the E-core FSPM motor section into nodes, b) heat flow diagram.

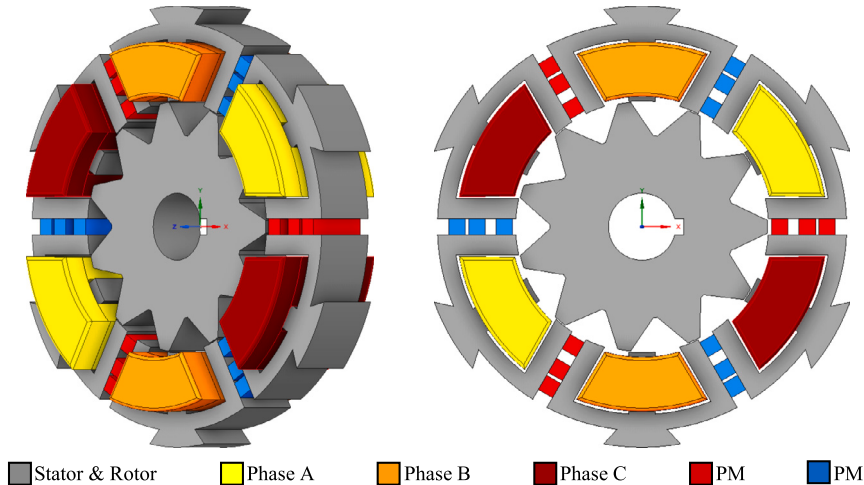


Fig. 4. Three-dimensional (left) and two-dimensional (right) views of the proposed motor. The red and blue colors of the PMs are utilized to show the anticlockwise and clockwise directions of the magnetic flux.

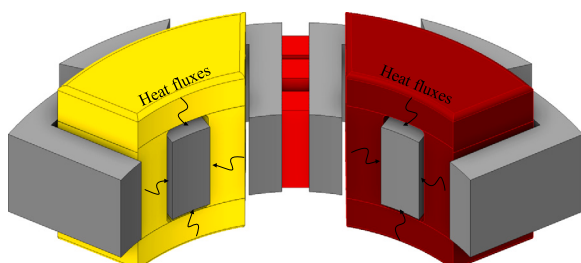


Fig. 5. Heat transfer paths from the active and end portion of the winding for the proposed motor.

Considering the blue loop and applying the KCL, the charging heat flow of the PM can be obtained as (4). Due to the insignificance of the released heat in the airgap region compared to the casing and surrounding ambient, similar to the thermal analysis of the E-core FSPM motor, the last two terms ($2Q_{to,ag}$ and $2Q_{mto,ag}$) are ignored. Therefore, the stored heat in the PM can be expressed as (5), which contains two sections. The first one, the active term, is similar to the E-core FSPM motor, while the term's coefficient is one. Therefore, the thermal impact of the active portion of the winding on the PM temperature is lower compared to that in the E-core FSPM motor. On the other hand, for the second term, not only is the coefficient of this term reduced to one, but there is also a significant heat transfer path to relieve the generated heat by passing

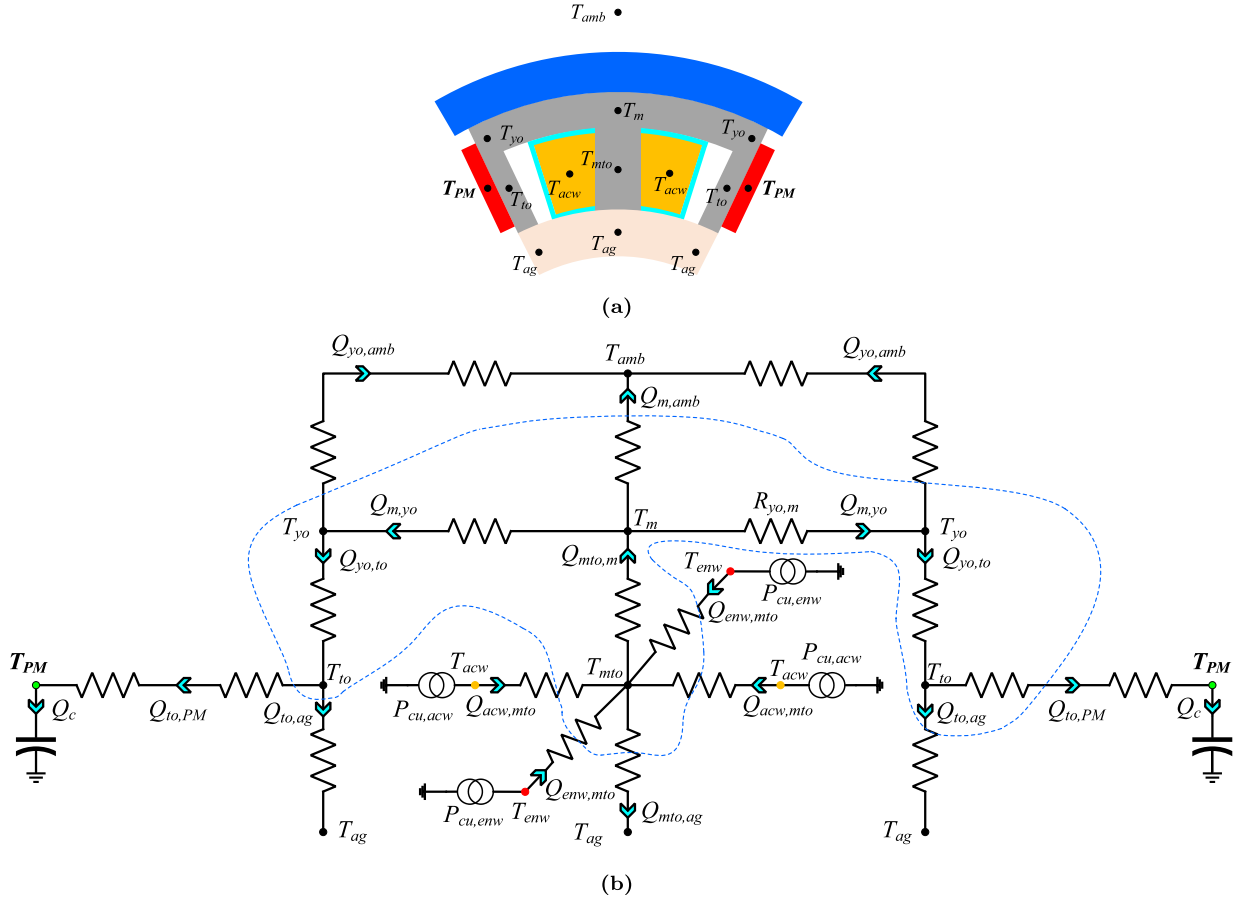


Fig. 6. a) Discretization of the proposed motor section into nodes, b) heat flow diagram.

it through the MT to the ambient ($0.5Q_{m,amb}$). Consequently, both heat flow terms are significantly lower than that of the E-core FSPM motor, and it can be revealed that, based on (6), the temperature rise of the PMs would be lower in the proposed motor.

$$2Q_c = 2Q_{acw,mto} + 2Q_{env,mto} - 2Q_{yo,amb} - Q_{m,amb} - 2Q_{to,ag} - Q_{mto,ag} \quad (4)$$

$$Q_c = \underbrace{Q_{acw,mto} - Q_{yo,amb}}_{\text{active term}} + \underbrace{Q_{env,mto} - 0.5Q_{m,amb}}_{\text{end term}} \quad (5)$$

The reduction in the heat flow from the hotspots to the PMs is projected in their temperature as expressed in (6), which includes additional subtractive terms compared to (3), as well as less weight for each of the additive terms.

$$T_{PM} = \frac{1}{C_p} \left[\int_0^{t_1} Q_{acw,mto}(t) dt + \int_0^{t_1} Q_{env,mto}(t) dt - \int_0^{t_1} Q_{yo,amb}(t) dt - \frac{1}{2} \int_0^{t_1} Q_{m,amb}(t) dt \right] \quad (6)$$

4. Numerical study

The heat transfer problem in electromagnetic systems is twofold: Firstly, the generated heat in the motor components, including the winding (copper), core, PMs, and bearings, should be comprehensively studied, as they are the motives behind the temperature rise. Secondly, the temperature distribution is pivotal to pinpoint the hotspots and apply appropriate strategies to mitigate them [42]. Thus, in the section, the heat generation and heat transfer problems are studied numerically using the FE analysis capabilities of ANSYS Electronics Desktop and ANSYS

Table 2
Thermophysical properties of materials.

Component	Material	ρ (kg.m^{-3})	λ ($\text{W.m}^{-1}.^{\circ}\text{C}^{-1}$)	C_p ($\text{J.kg}^{-1}.^{\circ}\text{C}^{-1}$)
Stator core	M350-50A steel	7650	30 (r), 4 (a)	460
Rotor core	M350-50A steel	7650	30 (r), 4 (a)	460
Winding	Copper	8933	401	385
Insulation	mixture	1150	0.17	1100
Casing	Aluminium	2790	168	833
Endcaps	Aluminium	2790	168	833
PM	NdFeB N30UH	8405.2	12	390

Fluent software packages to solve Maxwell's partial differential equations and heat transfer energy equation, respectively. To have a precise but fast response from the numerical study, the following assumptions are considered in the electromagnetic and thermal analyses.

1. The ambient temperature remains at the constant value of 25°C .
2. The contact thermal resistances between motor components are not considered.
3. The convection from the outer surface of the casing to the surrounding ambient is uniform.
4. The motor's thermal performance is studied under the nominal electromagnetic conditions, previously mentioned in Table 1.
5. Because of the low-speed application, Mechanical losses (windage, friction, and stray loss components) are neglected.
6. Thermophysical parameters of thermal conductivity, specific heat capacity, and density are considered constant, as mentioned in Table 2.
7. To consider the most stressful thermal conditions, the radiative heat transfer is considered zero.

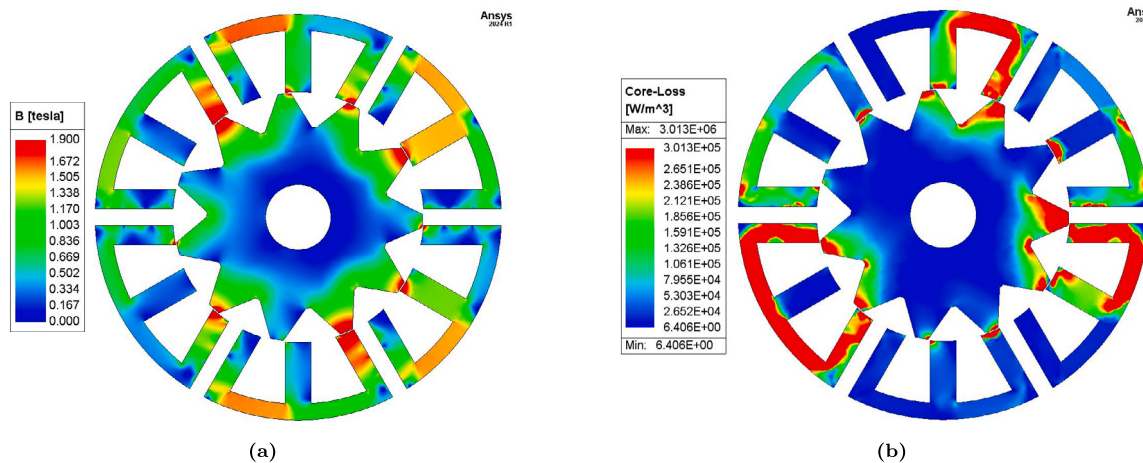


Fig. 7. Distribution of the a) flux density, and b) core losses in different regions of the stator and rotor cores of the E-core FSPM motor.

4.1. Heat generation

4.1.1. Copper losses

As a thermal reaction for the motor operation, power losses will be generated in the windings, steel cores, and PMs, which their summation is equivalent to the accumulated heat inside the motor. As previously described, for analysis, the winding can be divided into active and end parts, which their losses are known as joule (copper) losses. As indicated in (7), the copper losses contain DC and AC components, in which the former can be obtained from the geometrical properties of the winding and the root mean square of the armature current as (8) and (9) for a three-phase winding [43]. In the case of the AC copper losses, (10) is used to calculate them based on the physical/geometrical properties (D_m and R) of the winding, rotational speed (ω), and the maximum flux density (B_m). Although the FE calculations are required to calculate the B_m , the weight of the AC term is insignificant due to the presence of the square of wire diameter, D_m , which is only 0.65 mm for the E-core FSPM and proposed motors. Besides, the motors are operated under nominal states, where the low-speed, high-current region of the motor drive is utilized. Consequently, it can be reliably omitted, and the copper losses are calculated based on the DC component.

$$P_{cu} = \underbrace{P_{cu,acw} + P_{cu,enw}}_{P_{dc}} + P_{ac} \quad (7)$$

$$P_{cu,acw} = 3R_{acw}I_{rms}^2 = 3N \frac{\rho_{cu}L_{acw}}{A_{con}} I_{rms}^2 \quad (8)$$

$$P_{cu,enw} = 3R_{enw}I_{rms}^2 = 3N \frac{\rho_{cu}L_{enw}}{A_{con}} I_{rms}^2 \quad (9)$$

$$P_{ac} = \frac{\pi D_w^2 (\omega B_m)^2}{128 R} \quad (10)$$

In the E-core FSPM motor, the windings surround the PMTs and PMs, while in the proposed motor, they only revolve around the MT. Therefore, L_{enu} in the E-core FSPM motor is higher than the proposed motor under the same number of turns for coils (N). It is calculated that the volume of the end winding in the former is approximately 30% higher than that in the latter, which is obviously reflected in their copper losses, as indicated in Table 3. This phenomenon affects both electromagnetic and thermal performances, where the reduced losses eventuate in higher efficiency of the motor and a more comfortable hotspot, which results in temperature mitigation across the motor.

4.1.2. Core losses

The well-known Bertotti model as (11) is used to calculate the hysteresis, eddy, and excess components of the core losses, in which the

Table 3

Average generated heat in different regions of the E-core FSPM and proposed motors.

Component	Steel cores (W)	Winding (W)	PM (W)
E-core FSPM	15.9	40.7	0.011
Proposed	8.3	31.3	0.021

coefficients of k_{hyst} , k_{eddy} , and k_{exc} are estimated from the power loss-flux density curves of the M350-50A steel considering various frequencies [44]. As the maximum flux density, B_m , is required to calculate the core losses, the FE analysis is used to achieve the distribution of them in the stator and rotor cores for each time step. They are indicated in Figs. 7(a), 8(a) for the E-core FSPM and proposed motors, respectively. It is evident that the saturation level of the core is relatively higher in the E-core FSPM motor, which is due to the fact that the source of electrical and magnetic loadings are very close to each other in this motor. Therefore, their electromagnetic flux densities are in parallel, simultaneously appearing in the core and causing multiple saturating regions. However, in the proposed motor, the electrical loading sources are located around the MTs, and the magnetic ones are sandwiched between the PMTs. As a result, their flux densities act in different core regions, which, besides lower saturation, bring a much more uniform flux density distribution.

$$P_{core} = k_{hvst} B_m^\alpha f + k_{eddv} B_m^2 f^2 + k_{exc} B_m^{1.5} f^{1.5} \quad (11)$$

Because of the higher saturation level, the core losses of the E-core FSPM are significantly higher than the proposed motor, as demonstrated in Figs. 7(b), 8(b). In addition to the higher uniformity of the core losses in the stator and rotor cores of the proposed motor, the average power losses are lower compared to the E-core FSPM motor, which is reflected in Table 3. Therefore, quite similar to the copper losses, the reduction in the core losses in the proposed motor eventuates in higher efficiency and a decline in the overall temperature.

4.1.3. PM eddy current losses

Despite the fact that the stator and rotor cores are laminated in the axial direction to minimize the core's eddy current losses, in the PMs, the laminating is not thoroughly possible and accessible due to the lack of appropriate manufacturing technologies. Rather than laminating, in this study, for both the E-core FSPM and proposed motors, the PM is divided into three equal pieces to minimize the eddy current losses. Therefore, eddy currents will be generated inside the PMs due to the electromagnetic induction responsible for the PM losses. These losses are calculated from (12) according to the geometrical and material properties of the PM, as well as the current density through it [45].

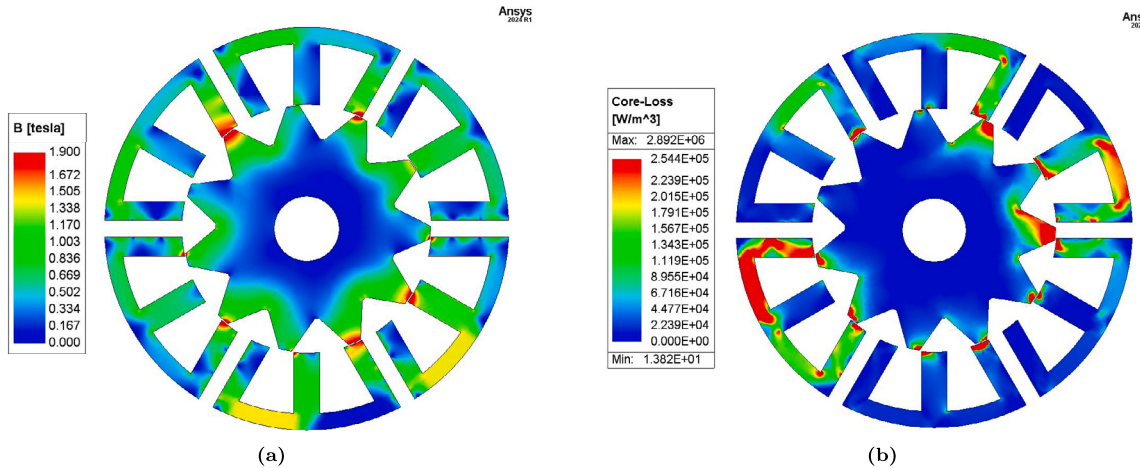


Fig. 8. Distribution of the a) flux density, and b) core losses in different regions of the stator and rotor cores of the proposed motor.

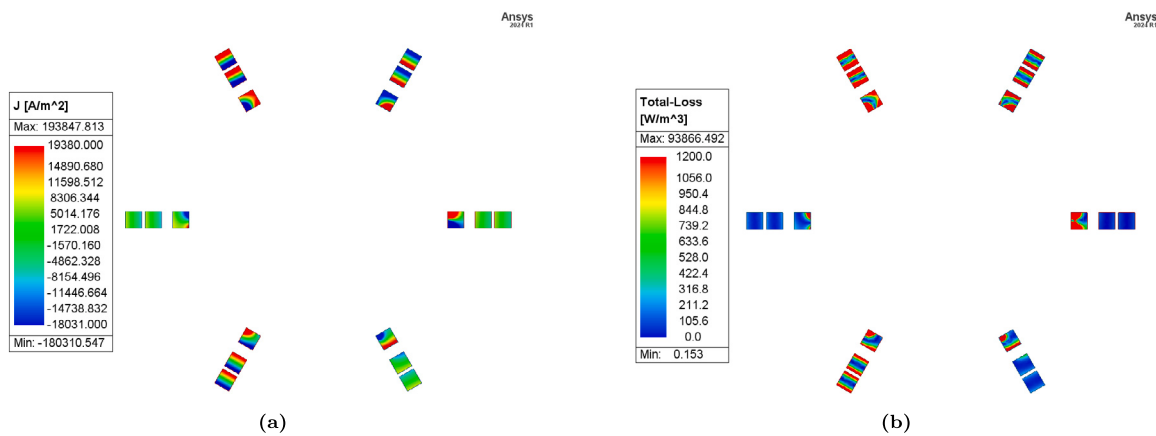


Fig. 9. Distribution of the a) current density, and b) eddy current losses in different regions of the PMs of the E-core FSPM motor.

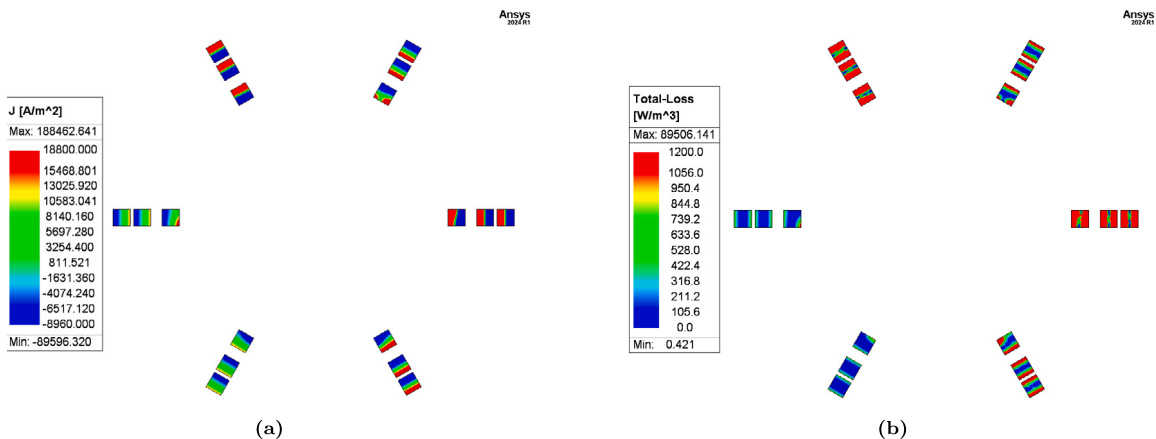


Fig. 10. Distribution of the a) current density, and b) eddy current losses in different regions of the PMs of the proposed motor.

$$P_{eddy} = \sum_V \int \frac{|J_v|^2}{2\sigma_{PM}} dV_{PM} \quad (12)$$

The eddy current densities across the PMs in the E-core FSPM and proposed motors are calculated using FE analysis and are demonstrated in Figs. 9(a) and 10(a). The PM eddy current losses in the different regions of the PMs track the intensity of the eddy current completely for both motors in Figs. 9(b) and 10(b). Where the absolute value of the current density has high intensity, the same pattern is observable in the PM

eddy current losses, while for the opposite, the losses are also insignificant. The average PM losses of both motors are mentioned in Table 3, which are insignificant compared to the other loss components.

4.2. Heat transfer

4.2.1. Thermal modeling

In the numerical thermal studies, the conjugate heat transfer should be investigated by incorporating the fluids and solids in the analysis.

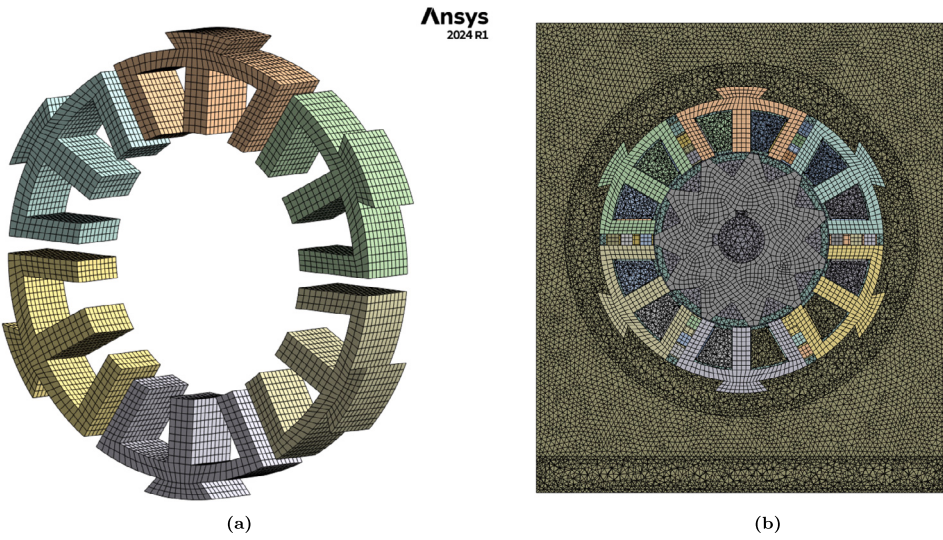


Fig. 11. Meshing of the a) stator blocks and b) motor components (radial-circumferential view).

Table 4
Convection HTC for different methods of cooling.

Cooling method	Required HTC (W.m ⁻² .°C ⁻¹)
Natural convection of gases	5-10
Forced convection of gases	10-250
Convection through liquids	50-20000
Boiling and condensation	2500-100000

However, in this study, the fluids are replaced by their equivalent convection HTC for the heat transfer from the motor casing to the ambient, and thermal conductivity for the heat transfer in the airgap region. For the surrounding ambient, to be compatible with the experimental study, the accumulated heat on the outer surface of the casing is collected through natural convection, where the HTC is considered 10 W.m⁻².°C⁻¹, based on Table 4 [46]. The motor is totally enclosed, and to have the worst thermal conditions, the value of the heat dissipation coefficient between end winding and end caps is considered zero (Neumann/adiabatic boundary condition). The same is the case for the heat transfer between the vertical end surfaces of the stator and rotor with end caps. Besides, the shaft is considered non-dissipative, and therefore, the only path for the rotor components to transfer their generated heat is the airgap. The thermal characteristics of the airgap are critical as the thermal connection between the stator and rotor is through this narrow region. The circulating flow in the smooth annular airgap subjected to inner cylinder rotation is considered completely radial flow with an equivalent thermal conductivity, which is calculated based on (13) to consider the self-ventilation effect of the rotor rotation on the temperature [47,48].

$$\lambda_{eq,Airgap} = 0.0019\eta^{-2.9084} Re^{0.461 \ln(3.3361\eta)}, Re = \frac{r_{os}\omega\delta}{v}, \eta = \frac{r_{os}}{R_{is}} \quad (13)$$

The stator and rotor cores are laminated in the axial direction to decrease the eddy current losses, and there is a substantial amount of glue between the laminations. Therefore, the heat transfer in the radial direction (r) is so much higher than the axial component (a), which means that the orthotropic thermal conductivities are calculated based on (14) in the axial direction and applied in the numerical studies (stator and rotor core in Table 2.) The winding is modeled as a homogeneous conductor with a uniform heat source, and an equivalent insulation layer is considered as the combination of slot insulation, impregnation, and residual air [19], where their equivalent thermal properties are calculated with (14).

$$\lambda_{eq} = \frac{\sum_{i=1}^m L_i}{\sum_{i=1}^m \frac{L_i}{\lambda_i}}, C_{p,eq} = \frac{\sum_{i=1}^m M_i C_i}{\sum_{i=1}^m M_i}, \rho_{eq} = \frac{\sum_{i=1}^m M_i}{A \sum_{i=1}^m L_i} \quad (14)$$

4.2.2. Mesh independence study

When the CFD is applied through the FE method to solve the heat transfer equations, such as the energy equation of (15), the whole problem region must be discretized to numerous partitioned elements, including nodes, lines, and surfaces. These equations are applied and solved in each element, and the final result is achieved by considering all elements [49]. Therefore, the meshing concept is even applicable to complex geometries of the electric motors, however, the number and size of the elements should be selected suitably to attain the precise solution with the least computational burden. The mesh independence study or mesh sensitivity analysis aims to find the lightest mesh configuration from the computational perspective, where the precise heat transfer solution can be achieved in the shortest possible time [50]. Accordingly, the mesh size is varied within a range where the fine and coarse mesh structures can be studied, as indicated in Table 5 for the E-core FSPM motor.

As demonstrated, increasing the mesh size significantly impacts the number of nodes and elements, which will cause the meshing step to be time-efficient. Besides, the average element quality remains approximately the same for the fine and coarse mesh structures, proving the mesh structures' efficiency with the smaller number of nodes and elements. However, as indicated in the temperature columns of Table 5, the maximum winding temperature deviates from the precisely calculated value (approximately 107.5 °C) when the mesh size is greater than 2 mm. The worst-case scenario in meshing appears with the mesh size of 5 mm when, besides severe deviation of the windings' temperature, the average temperature of the PM differs from its actual value (41.7 °C). Therefore, having fewer nodes and elements despite creating a high-quality mesh causes the heat transfer solution to lose its precision. Consequently, in this study, to have an accurate temperature solution in addition to the least computational time and burden, the discretization structure with a mesh size of 2 mm is considered and implemented. For the regular shapes such as the stator blocks and permanent magnets, as indicated in Fig. 11, the structured mesh with hexahedral elements has been generated using ANSYS Meshing software, while it is evident from Fig. 11(b) that a combination of tetrahedral and hexahedral elements has resulted for the other components, which have more complex geometries. A similar procedure is implemented on the proposed motor to

Table 5
Mesh independence study for the E-core FSPM motor.

Mesh size (mm)	Number of nodes	Number of elements	Average element quality	Maximum winding temperature (°C)	Average PM temperature (°C)
0.5	1.849×10^6	8.398×10^6	0.840	107.562	41.210
1	5.787×10^5	2.726×10^6	0.835	107.380	41.025
1.5	4.651×10^5	2.024×10^6	0.833	107.472	41.379
2	3.589×10^5	1.753×10^6	0.833	107.502	41.428
2.5	3.339×10^5	1.671×10^6	0.833	106.857	41.781
3	3.293×10^5	1.631×10^6	0.833	106.165	41.702
3.5	3.271×10^5	1.614×10^6	0.833	106.291	41.678
4	3.222×10^5	1.603×10^6	0.833	105.916	41.476
4.5	3.209×10^5	1.600×10^6	0.833	105.254	41.925
5	3.1917×10^5	1.594×10^6	0.833	104.559	42.372

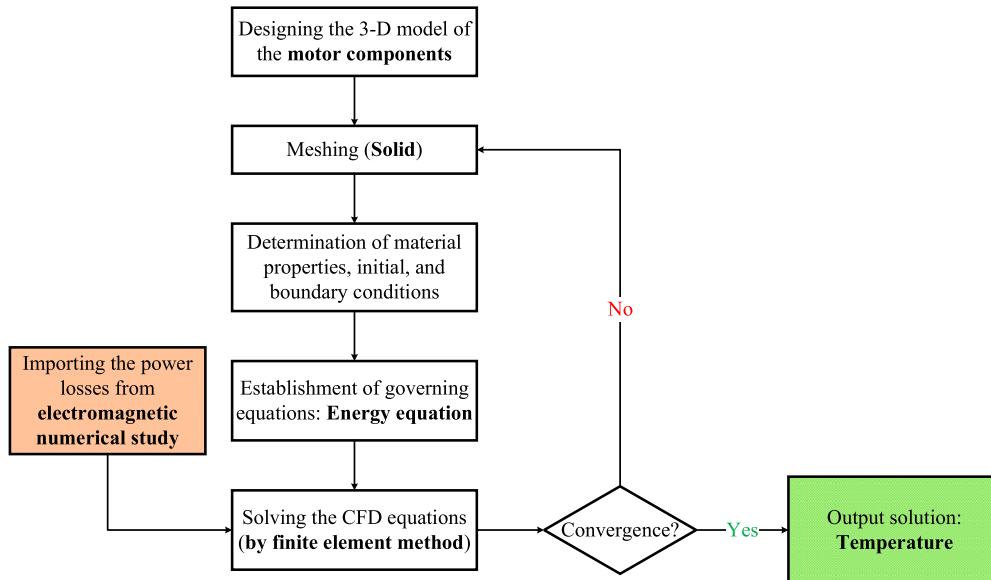


Fig. 12. The flowchart of numerical thermal study.

reach a fine mesh structure with accurate results and a light computational burden.

4.2.3. Thermal analysis

The flowchart of the numerical thermal study is indicated in Fig. 12. Starting from the three-dimensional modeling of the motor components, they will be discretized in the meshing step, and then the material properties and boundary conditions are assigned. To calculate the temperature distribution of the motor components, the energy equation of (15) is solved through the FE analysis, in which the heat generation inside the components is imported from the numerical electromagnetic study. When the residual value of the solution in the energy equation is 10^{-9} , the solution is judged as converged. Otherwise, in an iterative process, the meshing step should be modified appropriately, and the problem should be repeated until the convergence, after which the temperature of motor components can be extracted as the outcome.

$$\frac{\partial}{\partial x} \left(\lambda_x \frac{\partial T}{\partial x} \right) + \frac{\partial}{\partial y} \left(\lambda_y \frac{\partial T}{\partial y} \right) + \frac{\partial}{\partial z} \left(\lambda_z \frac{\partial T}{\partial z} \right) = -P + \rho C_p \left(\frac{\partial T}{\partial t} \right) \quad (15)$$

4.2.4. Numerical thermal results

Armature Windings: Comparing the results of the numerical thermal study in Figs. 13(a) (E-core FSPM motor), 14(a) (proposed motor), it is evident that due to the lower heat generation in the armature windings of the proposed motor (see Table 3), their temperature values are much lower than those in the E-core FSPM motor. Accordingly, the hotspot's temperature in the former is 68.6°C , while in the latter, it reaches values as high as 107.5°C . Besides increasing the resistivity of the windings

and the resultant copper loss intensification, such a temperature level may violate the specified threshold for the insulations, resulting in short-circuit faults.

PMs: Due to the specific location of the windings in the E-core FSPM motor, the accumulated heat in the hotspots will be released on the PMTs, which causes their temperature to increase as Fig. 13(b). However, in the proposed motor (Fig. 14(b)), the generated heat of the windings will be transferred to the MTs rather than the PMTs. Therefore, the maximum working temperature of the PMs in the proposed motor is approximately half that in the E-core FSPM motor, as demonstrated in Figs. 13(c), 14(c). Moreover, in both motors, the PMs near the airgap have relatively higher temperature values than those near the motor casing because of higher thermal resistance between the former and the ambient. It is obvious that mitigating the temperature of the stator side in the proposed structure has been projected to the rotor side. However, as indicated in Figs. 13(d), 14(d), the average temperature of the rotor in the proposed motor is only 3°C lower than the E-core FSPM motor. Therefore, compared to the stator temperature mitigation, the improvement of the heat transfer paths in the proposed motor has not such a significant effect on the rotor temperature, which is due to the presence of the airgap with much higher thermal resistance compared to the motor components. Considering the temperature of armature windings and PMs, this study verifies the analyses of the heat flow diagram.

5. Experimental verification

The results of the numerical thermal study are verified by the experimental tests on the proposed motor, which is manufactured and

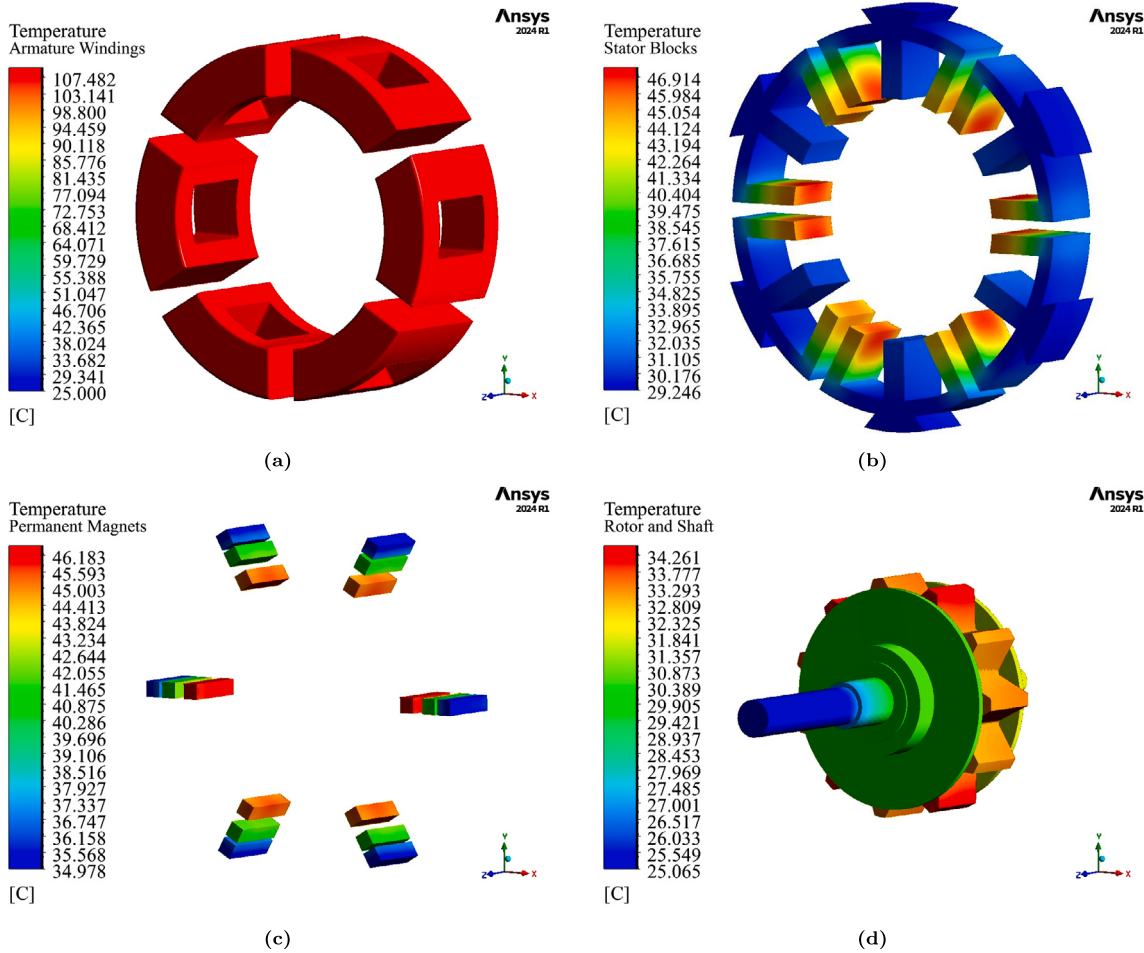


Fig. 13. FE study results for the temperature distribution of a) windings, b) stator blocks, c) PMs, and d) rotor and shaft in the E-core FSPM motor.

demonstrated in Fig. 15. On the stator side, besides the PMs, windings, and stator blocks, there is a motor casing with its screws to fix the stator blocks. Moreover, the holding layers between the PMTs and MTs serve as holders for the armature windings. To investigate the thermal performance under load, the test setup of Fig. 16 is implemented in the lab. In the experiments, the magnetic clutch provides the required motor load, and a three-phase voltage-source inverter feeds the armature windings. The applied electromagnetic torque on the motor shaft is transmitted through a torque transducer while the current probes monitor the load currents. Four drive steps, including 25%, 50%, 75%, and full load states, are applied continuously to examine the thermal performance. In the full load conditions, it is possible to verify the results of the previously presented numerical thermal study, while the other loading states are utilized for further verifications.

Based on the limitations in the lab, three Pt100 RTDs with an accuracy of 0.1°C and a temperature range of $[0\ 850]^{\circ}\text{C}$ are used to measure the temperature of windings, and ambient. The first sensor (No. 14 in Fig. 16) is inserted in the winding section through a hole in the front endcap to provide temperature data of the windings for verification of the numerical studies. The second Pt100 RTD is located near the motor surface in the surrounding ambient, where it can demonstrate the natural convection heat transfer from the motor surface to the ambient. Finally, the third sensor is located in the ambient farther than the second one to decide whether its temperature is constant. In collaboration with the MAX 31865 analog-to-digital converter, the Arduino Uno processor unit has been used to process the temperature data of three Pt100 RTD sensors. The processed data is transmitted to a PC through serial ports to monitor the temperature profile as a first-order dynamic system.

Table 6

The temperature of the winding in the numerical and experimental studies.

Component	25% loading	50% loading	75% loading	Full load
Numerical ($^{\circ}\text{C}$)	37.5	47.7	56.3	68.6
Experimental ($^{\circ}\text{C}$)	35.7	45.2	53.5	65.5
Error (%)	5	5.5	5.2	4.7

5.1. Experimental thermal results

The experimental temperature profiles of the Pt100 RTDs are indicated in Fig. 17. Based on the observations during the test and temperature dynamics, the measurements are conducted with a sampling frequency of 1 Hz for about 50 minutes, in which the first 2800 seconds are devoted to the active operation and heating phase of the motor, while the remaining is an indicator for the cooling performance during the downtime. During the heating phase, firstly, by applying the initial loading step (25%), the achieved temperature after 900 seconds is recorded. The same procedure is repeated for the 50% and 75% loadings, for which their temperature values are saved after 1600 seconds and 2200 seconds. Finally, the full loading state is applied and the motor's operation continues until the steady-state conditions. The results of the experimental and numerical studies for the winding's temperature are compared in Table 6, where the data is bolded for the full-load operation, for which the numerical results were provided in the previous section.

The results show that the maximum error between the experimental and numerical studies for different loading steps is below 6%, which is due to the assumptions of the numerical study. For instance, in the

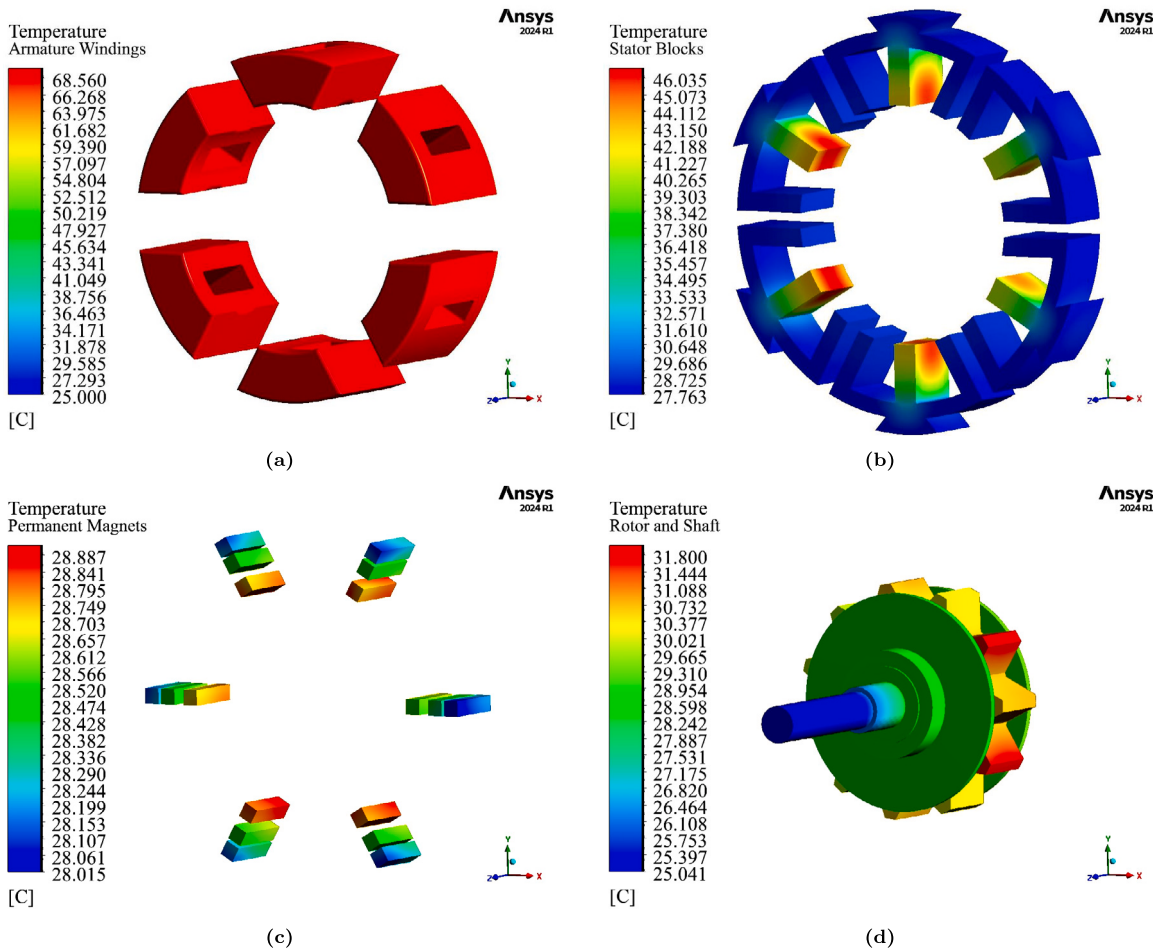


Fig. 14. FE study results for the temperature distribution of a) windings, b) stator blocks, c) PMs, and d) rotor and shaft in the proposed motor.

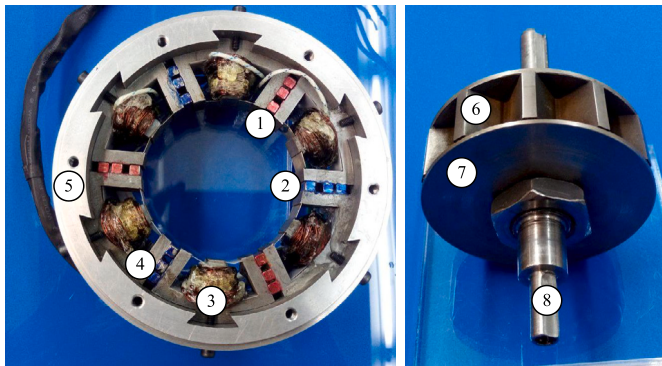


Fig. 15. Structure of the motor, including 1) positive-flux PM, 2) negative-flux PM, 3) armature winding, 4) stator block, 5) casing, 6) rotor, 7) rotor plate, and 8) shaft.

numerical studies for simplification, it was assumed that the motor is totally enclosed, for which there is no fluid interaction between the internal and external zones, while in the manufacturing phase, it is impossible to provide these conditions altogether. Therefore, some parts of the generated heat inside the motor are released to the ambient through tiny gaps thereby, the experimental results are relatively lower than the numerical ones. Upon rotation, the temperature of the surrounding ambient's sensor starts to escalate, which shows the natural convection heat transfer from the motor surface to the ambient, while the third sensor shows an approximately constant profile for the temperature of the far-away ambient. After 2800 seconds, the motor stops operation, and as

indicated, the temperature of the windings falls immediately. However, The accumulated heat inside them finds its way through the stator blocks and casing and is released to the surrounding environment, which is the reason behind the sudden increase in the ambient temperature, indicated in the cooling phase of Fig. 17.

6. Electromagnetic performance

Although the thermal performance of the proposed motor is demonstrated to be much better than the E-core FSPM motor, and the thermal stress experienced by the PMs has been mitigated considerably, the primary purpose of designing such motors is to deliver stable electromagnetic torque. In previous sections, the power losses of the motors were compared, which gives an indispensable insight into their efficiency. In this section, the electromagnetic performance is discussed further to investigate the qualifications of the proposed motor.

The operation of the motor should be described from a generator-oriented perspective to comprehend the electromechanical energy conversion. A linear arrangement is developed to facilitate the intuitive idea of energy conversion for the proposed motor, as shown in Fig. 18(a). Four different statuses of the element placement around a coil are shown, in which the MT of the E-core block and the rotor tooth are perfectly aligned in position (A), causing the flux linkage to experience the maximum. The flux linkage of the coil becomes zero at position (B) as a result of the complete misalignment, as shown by the corresponding curve in Fig. 18(b). For the PM flux to pass through completely, a full channel must be established in position (C) as soon as one electrical period is over. Due to the flux going from the stator to the rotor, the flux linkage reaches its maximum value where the polarity is the same

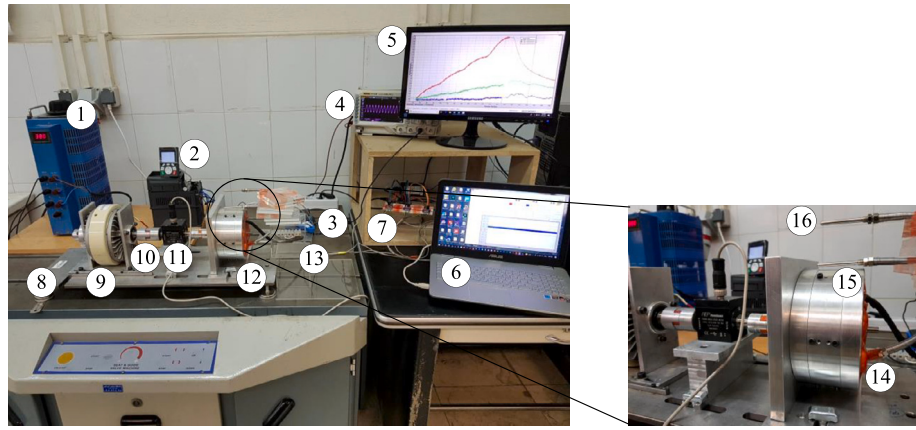


Fig. 16. Thermal test setup for temperature measurements on the proposed motor. 1) input power source, 2) 3-phase voltage source inverter, 3) current probe, 4) input current monitoring, 5) temperature monitoring, 6) electromagnetic torque monitoring, 7) temperature measurement unit, 8) test bench, 9) load (magnetic clutch), 10) mechanical coupling, 11) torque transducer, 12) proposed motor, 13) stand for temperature sensors, Pt100 RTD sensor for 14) end winding, 15) surrounding, and 16) ambient.

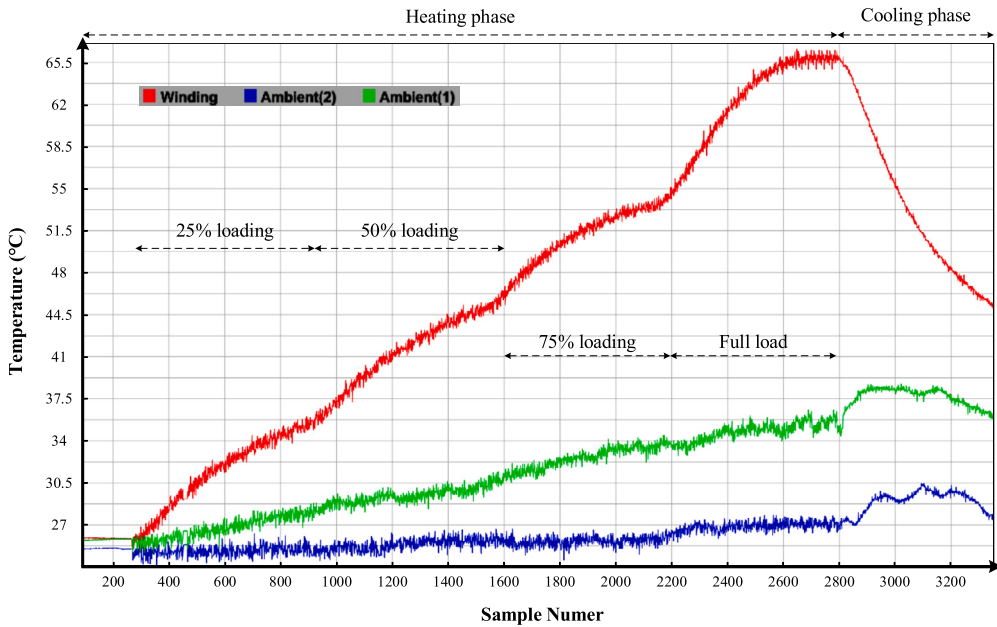


Fig. 17. Experimental temperature profiles of the winding, surroundings, and ambient.

as (A). Alternatively stated, each coil develops a unipolar flux linkage. As shown in Fig. 18(b), taking the derivative of the flux linkage results in the voltage induced in each coil in accordance with Faraday's law. Therefore, by properly connecting the various phase coils as Fig. 19, a symmetric sinusoidal voltage can feed the windings to deliver stable electromagnetic torque.

Applying armature current with a peak value ranging from 0 A to 15 A, the average electromagnetic torque of the E-core FSPM and proposed motors are calculated with the FE analysis and indicated in Fig. 20(a). When the underloading is the case ($I_{max} < 6$ A), both motors deliver electromagnetic torque values, for which the average is very close, while after the nominal point (6 A), the difference between them increases significantly. As previously indicated in Figs. 7(a), 8(a), the saturation level of the E-core FSPM motor is considerably higher than that of the proposed motor in the nominal operation. This level is intensified for the overload states ($I_{max} > 6$ A), which deteriorates the performance of the E-core FSPM motor, while the effect of the saturation on the performance of the proposed motor is much lower. The transient electromagnetic torque profile of the motors for the nominal operation is

demonstrated in Fig. 20(b), which indicates a higher average torque for the proposed motor (1.2 N.m) compared to the E-core FSPM motor (0.96 N.m).

6.1. Experimental electromagnetic results

The prototype of the proposed motor is tested under the rated load, as depicted in Fig. 21, which represents the test setup, including the motor, inverter (drive), load, and torque/current measurement devices. The resultant back-EMF waveforms under the no-load test as Fig. 22(a) demonstrates that the motor can operate under BLAC driving mode. Therefore, feeding the windings with sinusoidal voltages, the input three-phase currents of the motor under nominal operation are presented in Fig. 22(b). As shown in Fig. 23, the average electromagnetic torque of the test results is somewhat less than the numerical results, which is due to the biasing of the torque transducer (-0.1 N.m in this case) and undesirable prototyping defects. Therefore, the experimental results verify the electromagnetic numerical results, and it can be concluded that besides the thermal performance, the proposed motor's electromagnetic performance exceeds the E-core FSPM motor.

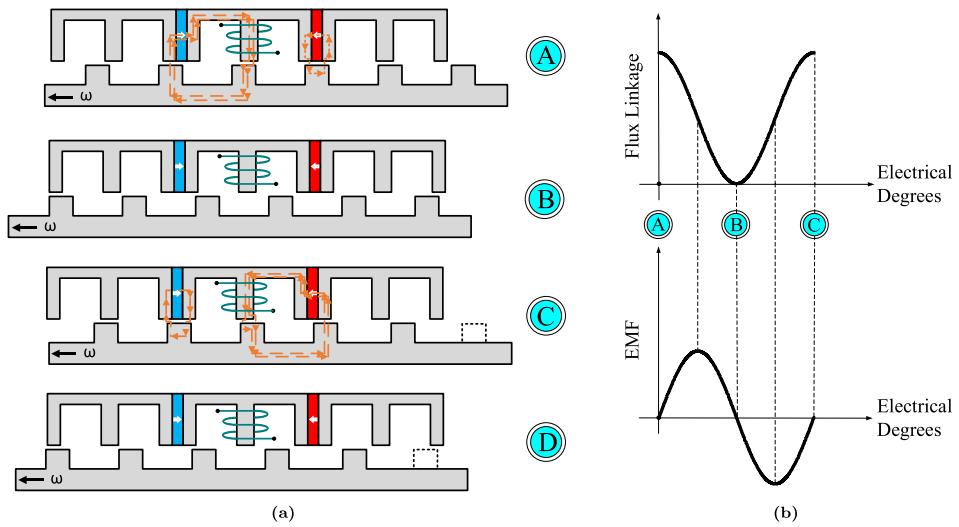


Fig. 18. Flux linkage a) in the motor structure and b) waveform in relation with the back-EMF of the proposed motor.

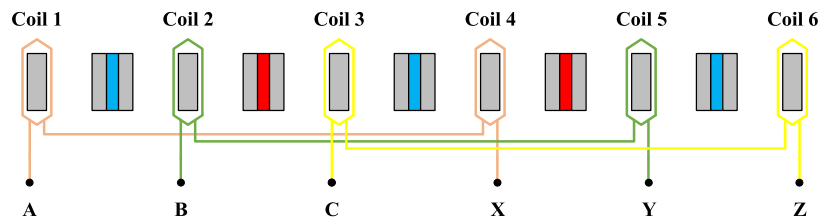


Fig. 19. Winding connections for the proposed motor.

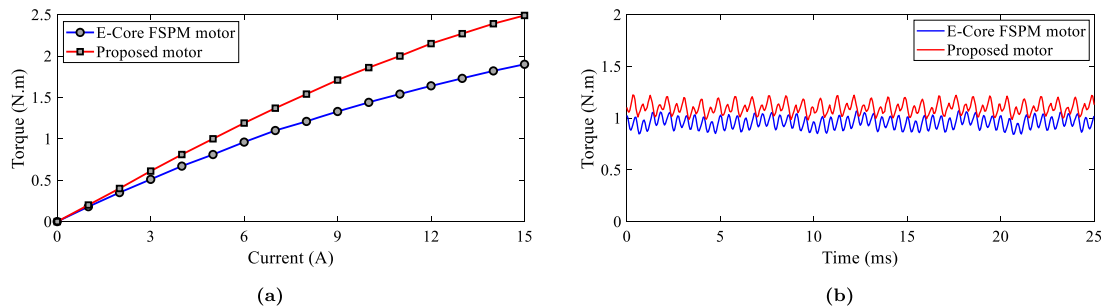


Fig. 20. Electromagnetic torque performance of the E-core FSPM and proposed motors a) versus armature current, b) transient profile.

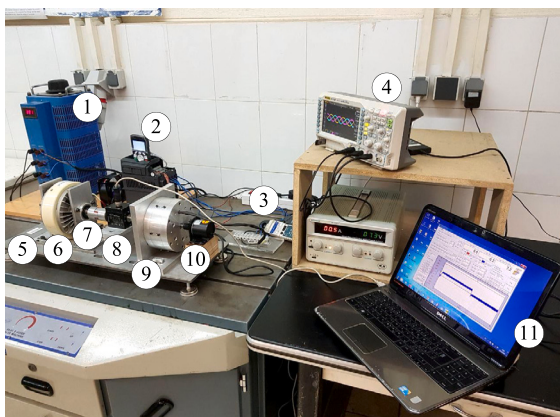


Fig. 21. Electromagnetic test setup for torque performance measurements on the proposed motor. 1) input power source, 2) 3-phase voltage source inverter, 3) current probes, 4) oscilloscope, 5) test bench, 6) load (magnetic clutch), 7) mechanical coupling, 8) torque transducer, 9) proposed motor, 10) encoder, and 11) electromagnetic torque monitoring.

6.2. Challenges of the proposed strategy

Generally, there are two challenges when applying the proposed strategy. As demonstrated in Fig. 1, in the E-core FSPM motor, the PMTs are surrounded by the armature windings, while the MTs' adjacency is empty. Therefore, as indicated in section 3 for the proposed motor, the armature windings evolved around the MTs to decrease the copper losses and heat transfer from the windings to the PMs. In better words, as there are free spaces in the surroundings of the MTs of the E-core FSPM motor, the heat transfer concepts can be utilized to modify the motor structure in order to have better electromagnetic and thermal performances. These free spaces are available in other structures of the FSPM motor, including the double-stator, double-rotor, and partitioned stator, and therefore, the proposed concept in this paper can be exploited to have better performances. The same is the case for permanent magnet synchronous motors (PMSMs) [51,52], switch reluctance motors (SRMs), brushless DC (BLDC) motors [53], and induction motors (IMs) [54,55]. However, in the classical structure of the FSPM motor, there are no MTs, but only PMTs which are entirely surrounded by the armature windings [56]. Accordingly, due to the lack of free space to

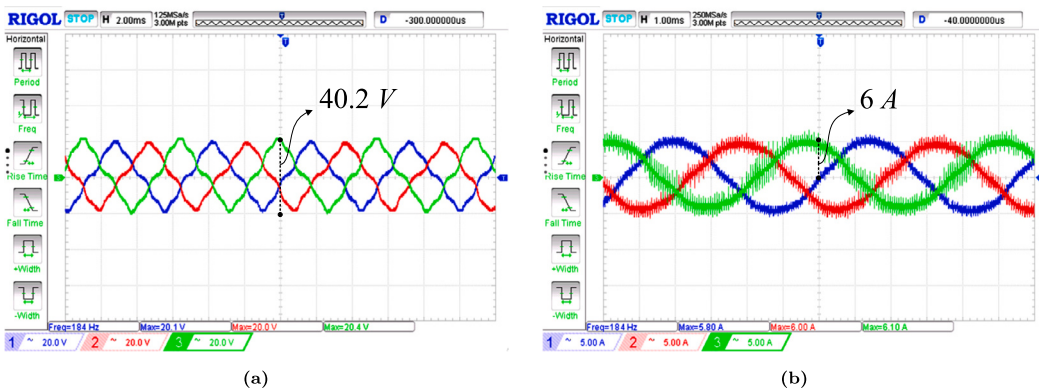


Fig. 22. Experimental three phase waveforms of a) back-EMF, and b) input current.

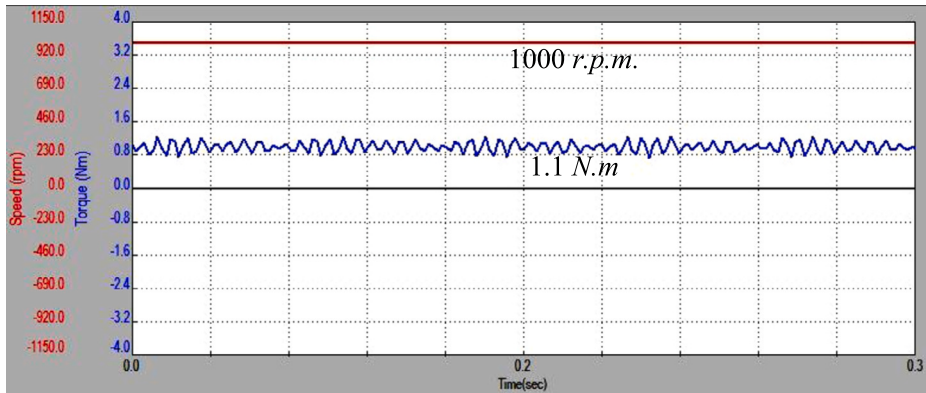


Fig. 23. Experimental profile of the electromagnetic torque and rotational speed of the proposed motor.

change the location of the armature windings, there are challenges to applying the proposed strategy of this study. Consequently, it can be stated that when the structure of the stator is already busy with the simultaneous presence of the PMs and armature windings, and there is no space to modify their locations, the proposed method is challenging to implement.

As indicated, after modifications in the structure of the E-core FSPM motor in section 2 to reach the proposed design and investigate the heat generation and heat transfer aspects of the problem, the electromagnetic performance of the motor is also discussed, and through finite element analysis, it is ensured that the proposed motor will deliver stable electromagnetic torque, which is much better compared to the E-core FSPM motor. It is possible that after modifying the structure to reach better thermal performance, the electromagnetic performance of the motor deteriorates, which causes challenges and indicates that the proposed structure is not feasible and cannot be manufactured. Therefore, after reaching a new design, the electromagnetic analysis should be carried out, in addition to the thermal study, to ensure the machine's performance.

7. Conclusions

In this study, a new approach was presented to mitigate the temperature of the PMs and armature windings in the structure of the E-core FSPM motor. Not only did the proposed strategy decrease the hotspot and PM temperature levels, but it also guided the structural parameters in the direction of generating fewer power losses, benefiting the efficiency and electromagnetic performance of the proposed motor. From the thermal perspective, as the PMs are sandwiched between the PMTs, placing the armature windings around the MTs rather than the PMTs had the following advantages in the heat generation and heat transfer stages:

1. The volume of the end part of the windings was decreased by 30%, which was reflected in the copper losses reduction from 40.7 W to 31.3 W. Besides the generated heat, the temperature of the armature windings in the proposed motor has been decreased by approximately 40 °C compared to the E-core FSPM motor.
2. The separation between the electrical and magnetic loading sources has caused a significant decline in the saturation level of the stator and rotor cores, which resulted in fewer core losses for the proposed motor.
3. In the E-core FSPM motor, the generated heat in the end part of the windings was transferred to the PMs entirely, while in the proposed motor, the MTs were the destination of the copper losses. In the former, the temperature of the PMTs on both sides of the PMs is about 45 °C, while in the proposed motor, the temperature of the MTs is at the same level, which is far away from the PMs, and therefore, the maximum PM temperature approximately cut by half in the proposed motor.

The results of the analytical and numerical studies were approved by the thermal experiments using three Pt100 RTD sensors for the windings, surrounding ambient, and environment, for which the error was less than 6%. From the electromagnetic perspective, the proposed motor outperformed the E-core FSPM motor in the nominal loading region due to the separation between the electromagnetic fluxes of the armature windings and PMs, which resulted in a uniform distribution of the flux density. These superiorities became much more prominent in the overloading, where the saturation level in the E-core FSPM motor caused a severe deterioration in the electromagnetic torque. Consequently, modifying the heat transfer path can be reliably used as a new approach to alleviating the temperature of PM motors, provided that the electromagnetic performance is at least at the same level as the initial motor. With the considerable advancement in materials and manufacturing technolo-

gies, additive manufacturing is revolutionizing the electrical machines' design procedure. Accordingly, topology optimization can be implemented in the proposed structure to further improve the electromagnetic and thermal performances. Besides, incorporating the advanced materials through additive manufacturing can be utilized to strengthen the heat transfer from the windings to the surrounding environment.

CRediT authorship contribution statement

Tohid Sharifi: Writing – review & editing, Writing – original draft, Validation, Software, Methodology, Formal analysis, Conceptualization.

Alireza Eikani: Writing – review & editing, Validation, Investigation, Conceptualization.

Funding

No funding was received for conducting this study.

Declaration of competing interest

The authors declare that they have no known competing financial interests or personal relationships that could have appeared to influence the work reported in this paper.

Data availability

Data will be made available on request.

References

- [1] J.A.P. Selvin Raj, L.G. Asirvatham, A.A. Angeline, S. Manova, B.L. Rakshith, J.R. Bose, O. Mahian, S. Wongwises, Thermal management strategies and power ratings of electric vehicle motors, *Renew. Sustain. Energy Rev.* 189 (2024) 113874, <https://doi.org/10.1016/j.rser.2023.113874>, <https://www.sciencedirect.com/science/article/pii/S1364032123007323>.
- [2] S.W. Chang, P.-S. Wu, Y.-S. Hong, Y.-C. Hsu, S.-H. Huang, Thermal characterization of an interior permanent magnet electric motor, *Results Eng.* 20 (2023) 101540, <https://doi.org/10.1016/j.rineng.2023.101540>, <https://www.sciencedirect.com/science/article/pii/S2590123023006679>.
- [3] Z. Feng, S. Zhao, W. Gao, Y. Zhang, L. Fei, Study on a novel in-wheel motor driving system driven by two permanent magnet synchronous disc motors, *IEEE Trans. Veh. Technol.* 72 (5) (2023) 5922–5933, <https://doi.org/10.1109/TVT.2023.32233997>.
- [4] L. Cao, Y. Zuo, S. Xie, C.C. Hoang, B.S. Han, C.H.T. Lee, Comparative study of permanent-magnet vernier motor and interior permanent-magnet motor for hybrid electric vehicles, *IEEE Trans. Ind. Appl.* 59 (6) (2023) 6601–6614, <https://doi.org/10.1109/TIA.2023.3292813>.
- [5] X. Zhu, S. Li, S. Zheng, L. Quan, D. Fan, X. Zeng, C.H.T. Lee, Torque component redistribution and enhancement for hybrid permanent magnet motor with permanent magnet offset placement, *IEEE Trans. Transp. Electrif.* 9 (1) (2023) 631–641, <https://doi.org/10.1109/TTE.2022.3177745>.
- [6] R. Hughes, T. Haidinger, X. Pei, C. Vagg, Real-time temperature prediction of electric machines using machine learning with physically informed features, *Energy AI* 14 (2023) 100288, <https://doi.org/10.1016/j.egyai.2023.100288>, <https://www.sciencedirect.com/science/article/pii/S266654682300605>.
- [7] W. Kirchgässner, O. Wallscheid, J. Böcker, Thermal neural networks: lumped-parameter thermal modeling with state-space machine learning, *Eng. Appl. Artif. Intell.* 117 (2023) 105537, <https://doi.org/10.1016/j.engappai.2022.105537>, <https://www.sciencedirect.com/science/article/pii/S0952197622005279>.
- [8] D.F. de Souza, P.P.F. da Silva, I.L. Sauer, A.T. de Almeida, H. Tatizawa, Life cycle assessment of electric motors - a systematic literature review, *J. Clean. Prod.* 456 (2024) 142366, <https://doi.org/10.1016/j.jclepro.2024.142366>, <https://www.sciencedirect.com/science/article/pii/S0959652624018146>.
- [9] H. Dong, H. Ma, Z. Wang, J. Man, L. Jia, Y. Qin, An online health monitoring framework for traction motors in high-speed trains using temperature signals, *IEEE Trans. Ind. Inform.* 19 (2) (2023) 1389–1400, <https://doi.org/10.1109/TII.2022.3200357>.
- [10] T. Sharifi, A. Eikani, M. Mirsalim, Heat transfer study on a stator-permanent magnet electric motor: a hybrid estimation model for real-time temperature monitoring and predictive maintenance, *Case Stud. Therm. Eng.* (2024) 105286, <https://doi.org/10.1016/j.csite.2024.105286>, <https://www.sciencedirect.com/science/article/pii/S2214157X24013170>.
- [11] P. Liang, F. Chai, K. Shen, W. Liu, Water jacket and slot optimization of a water-cooling permanent magnet synchronous in-wheel motor, *IEEE Trans. Ind. Appl.* 57 (3) (2021) 2431–2439, <https://doi.org/10.1109/TIA.2021.3064779>.
- [12] Z. Li, W. Zhu, B. Wang, Q. Wang, J. Du, B. Sun, Optimization of cooling water jacket structure of high-speed electric spindle based on response surface method, *Case Stud. Therm. Eng.* 48 (2023) 103158, <https://doi.org/10.1016/j.csite.2023.103158>, <https://www.sciencedirect.com/science/article/pii/S2214157X23004641>.
- [13] W. Le, M. Lin, K. Lin, L. Jia, S. Wang, A rotor cooling enhanced method for axial flux permanent magnet synchronous machine with housing-cooling, *IEEE Trans. Appl. Supercond.* 31 (8) (2021) 1–5, <https://doi.org/10.1109/TASC.2021.3103728>.
- [14] S. Wu, D. Hao, W. Tong, Cooling system design and thermal analysis of modular stator hybrid excitation synchronous motor, *CES Trans. Electr. Mach. Syst.* 6 (3) (2022) 241–251, <https://doi.org/10.30941/CESTEMS.2022.00034>.
- [15] Y. Sun, S. Zhang, W. Yuan, Y. Tang, J. Li, K. Tang, Applicability study of the potting material based thermal management strategy for permanent magnet synchronous motors, *Appl. Therm. Eng.* 149 (2019) 1370–1378, <https://doi.org/10.1016/j.applthermaleng.2018.12.141>, <https://www.sciencedirect.com/science/article/pii/S1359431118332903>.
- [16] Z. Yu, Y. Li, Y. Jing, J. Wang, Cooling system of outer rotor spmsm for a two-seater all-electric aircraft based on heat pipe technology, *IEEE Trans. Transp. Electrif.* 8 (2) (2022) 1656–1664, <https://doi.org/10.1109/TTE.2021.3127555>.
- [17] J. Huang, S. Shoai Naini, R. Miller, D. Rizzo, K. Sebeck, S. Shurin, J. Wagner, A hybrid electric vehicle motor cooling system—design, model, and control, *IEEE Trans. Veh. Technol.* 68 (5) (2019) 4467–4478, <https://doi.org/10.1109/TVT.2019.2902135>.
- [18] N. Putra, B. Ariantara, Electric motor thermal management system using l-shaped flat heat pipes, *Appl. Therm. Eng.* 126 (2017) 1156–1163, <https://doi.org/10.1016/j.applthermaleng.2017.01.090>, <https://www.sciencedirect.com/science/article/pii/S1359431117305458>.
- [19] W. Geng, T. Zhu, Q. Li, Z. Zhang, Windings indirect liquid cooling method for a compact outer-rotor pm starter/generator with concentrated windings, *IEEE Trans. Energy Convers.* 36 (4) (2021) 3282–3293, <https://doi.org/10.1109/TEC.2021.3084507>.
- [20] E. Yousefi, A. Abbas Nejad, Waste heat management in electric motors using thermo-electric generator integrated with phase change material and metal foam-embedded heat sink, *Energy Rep.* 11 (2024) 6199–6207, <https://doi.org/10.1016/j.egyr.2024.06.009>, <https://www.sciencedirect.com/science/article/pii/S2352484724003652>.
- [21] X. Liu, Y. Shi, J. Chu, S. Xue, Q. Zhao, X. Wu, M. He, A new phase-change cooling method for the frequent start-stop electric motor, *Appl. Therm. Eng.* 198 (2021) 117504, <https://doi.org/10.1016/j.applthermaleng.2021.117504>, <https://www.sciencedirect.com/science/article/pii/S1359431121009364>.
- [22] J. Park, J. An, K. Han, H.-S. Choi, I. Seouk Park, Enhancement of cooling performance in traction motor of electric vehicle using direct slot cooling method, *Appl. Therm. Eng.* 217 (2022) 119082, <https://doi.org/10.1016/j.applthermaleng.2022.119082>, <https://www.sciencedirect.com/science/article/pii/S1359431122010146>.
- [23] M. Sun, Y. Xu, W. Zhang, Multiphysics analysis of flywheel energy storage system based on cup winding permanent magnet synchronous machine, *IEEE Trans. Energy Convers.* 38 (4) (2023) 2684–2694, <https://doi.org/10.1109/TEC.2023.3283504>.
- [24] K.S. Garud, M.-Y. Lee, Grey relational based Taguchi analysis on heat transfer performances of direct oil spray cooling system for electric vehicle driving motor, *Int. J. Heat Mass Transf.* 201 (2023) 123596, <https://doi.org/10.1016/j.ijheatmasstransfer.2022.123596>, <https://www.sciencedirect.com/science/article/pii/S0017931022010651>.
- [25] H. Wang, X. Liu, M. Kang, L. Guo, X. Li, Oil injection cooling design for the ipmsm applied in electric vehicles, *IEEE Trans. Transp. Electrif.* 8 (3) (2022) 3427–3440, <https://doi.org/10.1109/TTE.2022.3161064>.
- [26] M.H. Park, S.C. Kim, Development and validation of lumped parameter thermal network model on rotational oil spray cooled motor for electric vehicles, *Appl. Therm. Eng.* 225 (2023) 120176, <https://doi.org/10.1016/j.applthermaleng.2023.120176>, <https://www.sciencedirect.com/science/article/pii/S1359431123002053>.
- [27] H. Tiismus, A. Kallaste, T. Vaimann, A. Rassölklin, State of the art of additively manufactured electromagnetic materials for topology optimized electrical machines, *Addit. Manuf.* 55 (2022) 102778, <https://doi.org/10.1016/j.addma.2022.102778>, <https://www.sciencedirect.com/science/article/pii/S2214860422001828>.
- [28] Y.-H. Lin, M.-T. Lee, Y.-H. Hung, A thermal management control using particle swarm optimization for hybrid electric energy system of electric vehicles, *Results Eng.* 21 (2024) 101717, <https://doi.org/10.1016/j.rineng.2023.101717>, <https://www.sciencedirect.com/science/article/pii/S2590123023008447>.
- [29] T. Lamichhane, L. Sethuraman, A. Dalagan, H. Wang, J. Keller, M. Paranthaman, Additive manufacturing of soft magnets for electrical machines—a review, *Mater. Today Phys.* 15 (2020) 100255, <https://doi.org/10.1016/j.mtphys.2020.100255>, <https://www.sciencedirect.com/science/article/pii/S2542529320300791>.
- [30] K. Arole, M.J. Green, H. Liang, 11 - thermal and electrical properties of electric vehicle fluids, in: L.I. Farfan-Cabrera, A. Erdemir (Eds.), *Electric Vehicle Tribology*, Elsevier Series on Tribology and Surface Engineering, Elsevier, 2024, pp. 193–206, <https://www.sciencedirect.com/science/article/pii/B978044314074700011X>.
- [31] M. Broumand, S. Yun, Z. Hong, A novel phase change material-based thermal management of electric machine windings enabled by additive manufacturing, *Appl. Therm. Eng.* 244 (2024) 122802, <https://doi.org/10.1016/j.applthermaleng.2024.122802>, <https://www.sciencedirect.com/science/article/pii/S1359431124004708>.
- [32] T.A. Huynh, M.-F. Hsieh, Improvement of traction motor performance for electric vehicles using conductors with insulation of high thermal conductivity considering cooling methods, *IEEE Trans. Magn.* 57 (2) (2021) 1–5, <https://doi.org/10.1109/TMAG.2020.3021127>.

- [33] X. Li, D. Dietz, J. An, N. Erd, Y. Gemeinder, A. Binder, Manufacture and testing of a magnetically suspended 0.5-kWh flywheel energy storage system, *IEEE Trans. Ind. Appl.* 58 (5) (2022) 6152–6162, <https://doi.org/10.1109/TIA.2022.3187393>.
- [34] J. He, J. Hu, B. Zhou, H. Jia, X. Liu, Z. Zhang, L. Wen, L. Zhao, H. Yu, X. Zhong, X. Zhang, Z. Liu, Simultaneous enhancement of coercivity and electric resistivity of nd-fe-b magnets by pr-tb-al-cu synergistic grain boundary diffusion toward high-temperature motor rotors, *J. Mater. Sci. Technol.* 154 (2023) 54–64, <https://doi.org/10.1016/j.jmst.2023.03.001>, <https://www.sciencedirect.com/science/article/pii/S10050302223001755>.
- [35] K. Sandip Garud, M.-Y. Lee, Thermal management characteristics of electric vehicle driving motor with oil spray cooling based on spray locations and oil types, *Appl. Therm. Eng.* 248 (2024) 123234, <https://doi.org/10.1016/j.applthermaleng.2024.123234>, <https://www.sciencedirect.com/science/article/pii/S1359431124009025>.
- [36] J.S. Na, C.-M. Ryu, S.J. Moon, Thermal analysis methods for wound rotor synchronous motors with water-cooling jackets, *Therm. Sci. Eng. Prog.* 46 (2023) 102177, <https://doi.org/10.1016/j.tsep.2023.102177>, <https://www.sciencedirect.com/science/article/pii/S2451904923005309>.
- [37] P. Desevaux Guechi, P. Baucour, C. Espanet, R. Brunel, M. Poirot, Spray cooling of electric motor coil windings, *J. Comput. Multiph. Flows* 8 (2016) 95–100, <https://api.semanticscholar.org/CorpusID:123268058>.
- [38] E. Gundabattini, R. Kuppan, D.G. Solomon, A. Kalam, D. Kothari, R. Abu Bakar, A review on methods of finding losses and cooling methods to increase efficiency of electric machines, *Ain Shams Eng. J.* 12 (1) (2021) 497–505, <https://doi.org/10.1016/j.asej.2020.08.014>, <https://www.sciencedirect.com/science/article/pii/S2090447920301854>.
- [39] W. Zhou, X. Tang, J. Zhu, Design and optimal coolant flow rate analysis of an annular water-cooled automotive exhaust-based thermoelectric generator, *Case Stud. Therm. Eng.* 56 (2024) 104256, <https://doi.org/10.1016/j.csite.2024.104256>, <https://www.sciencedirect.com/science/article/pii/S2214157X24002879>.
- [40] W. Li, M. Cheng, Reliability analysis and evaluation for flux-switching permanent magnet machine, *IEEE Trans. Ind. Electron.* 66 (3) (2019) 1760–1769, <https://doi.org/10.1109/TIE.2018.2838105>.
- [41] L. Xu, X. Zhu, W. Fan, C. Zhang, L. Zhang, L. Quan, Comparative analysis and design of partitioned stator hybrid excitation axial flux switching pm motors for in-wheel traction applications, *IEEE Trans. Energy Convers.* 37 (2) (2022) 1416–1427, <https://doi.org/10.1109/TEC.2021.3130475>.
- [42] Losses and Heat Transfer, John Wiley & Sons, Ltd, 2013, pp. 523–569, Ch. 9, <https://onlinelibrary.wiley.com/doi/abs/10.1002/9781118701591.ch9>.
- [43] A. Tikadar, J.W. Kim, Y. Joshi, S. Kumar, Flow-assisted evaporative cooling for electric motor, *IEEE Trans. Transp. Electrif.* 8 (1) (2022) 1128–1143, <https://doi.org/10.1109/TTE.2021.3107505>.
- [44] Y. Liu, J. Cao, Y. Song, Z. Gao, L. Li, Analysis of the immersion cooling of electric motors for hybrid aircraft, *Process Saf. Environ. Prot.* 178 (2023) 695–705, <https://doi.org/10.1016/j.psep.2023.08.067>, <https://www.sciencedirect.com/science/article/pii/S0957582023007784>.
- [45] W. Shi, X. Zhou, Online estimation method for permanent magnet temperature of high-density permanent magnet synchronous motor, *IEEJ Trans. Electr. Electron. Eng.* 15 (5) (2020) 751–756, <https://doi.org/10.1002/tee.23111>, <https://onlinelibrary.wiley.com/doi/abs/10.1002/tee.23111>.
- [46] P. König, D. Sharma, K.R. Konda, T. Xie, K. Höschler, Comprehensive review on cooling of permanent magnet synchronous motors and their qualitative assessment for aerospace applications, *Energies* 16 (22) (2023), <https://doi.org/10.3390/en16227524>, <https://www.mdpi.com/1996-1073/16/22/7524>.
- [47] Q. Chen, H. Shao, J. Huang, H. Sun, J. Xie, Analysis of temperature field and water cooling of outer rotor in-wheel motor for electric vehicle, *IEEE Access* 7 (2019) 140142–140151, <https://doi.org/10.1109/ACCESS.2019.2943775>.
- [48] X. Wang, B. Li, D. Gerada, K. Huang, I. Stone, S. Worrall, Y. Yan, A critical review on thermal management technologies for motors in electric cars, *Appl. Therm. Eng.* 201 (2022) 117758, <https://doi.org/10.1016/j.applthermaleng.2021.117758>, <https://www.sciencedirect.com/science/article/pii/S1359431121011820>.
- [49] S. Wang, Y. Li, Y.-Z. Li, J. Wang, X. Xiao, W. Guo, Transient cooling effect analyses for a permanent-magnet synchronous motor with phase-change-material packaging, *Appl. Therm. Eng.* 109 (2016) 251–260, <https://doi.org/10.1016/j.applthermaleng.2016.08.036>, <https://www.sciencedirect.com/science/article/pii/S1359431116313825>.
- [50] S. Motaman, M. Eltaweel, M.R. Herfatmanesh, T. Knichel, A. Deakin, Numerical analysis of a flywheel energy storage system for low carbon powertrain applications, *J. Energy Storage* 61 (2023) 106808, <https://doi.org/10.1016/j.est.2023.106808>, <https://www.sciencedirect.com/science/article/pii/S2352152X23002050>.
- [51] F. Chen, J. Fan, W. Li, J. Fang, S. Ding, Mitigation of high-resistance connection in surface-mounted pmsm drive system based on model predictive current control, *Results Eng.* 15 (2022) 100590, <https://doi.org/10.1016/j.rineng.2022.100590>, <https://www.sciencedirect.com/science/article/pii/S2590123022002602>.
- [52] H. Djouadi, K. Ouari, Y. Belkhier, H. Lehouche, M. Bajaj, V. Blazek, Improved robust model predictive control for pmsm using backstepping control and incorporating integral action with experimental validation, *Results Eng.* 23 (2024) 102416, <https://doi.org/10.1016/j.rineng.2024.102416>, <https://www.sciencedirect.com/science/article/pii/S2590123024006716>.
- [53] M. Megrini, A. Gaga, Y. Mehdaoui, Processor in the loop implementation of artificial neural network controller for bldc motor speed control, *Results Eng.* 23 (2024) 102422, <https://doi.org/10.1016/j.rineng.2024.102422>, <https://www.sciencedirect.com/science/article/pii/S2590123024006777>.
- [54] M.F. Yakhni, S. Cauet, A. Sakout, H. Assoum, E. Etien, L. Rambault, M. Ali, M. El-Gohary, Induction motor tacholess fault detection in transient speeds using adaptive generalized Vold Kalman filter, *Results Eng.* 24 (2024) 102961, <https://doi.org/10.1016/j.rineng.2024.102961>, <https://www.sciencedirect.com/science/article/pii/S2590123024012167>.
- [55] X. Chi, C. Wang, Q. Wu, J. Yang, W. Lin, P. Zeng, H. Li, M. Shao, A ripple suppression of sensorless fcc of pmsm electrical drive system based on mras, *Results Eng.* 20 (2023) 101427, <https://doi.org/10.1016/j.rineng.2023.101427>, <https://www.sciencedirect.com/science/article/pii/S2590123023005546>.
- [56] W. Hua, M. Cheng, Z.Q. Zhu, D. Howe, Analysis and optimization of back emf waveform of a flux-switching permanent magnet motor, *IEEE Trans. Energy Convers.* 23 (3) (2008) 727–733, <https://doi.org/10.1109/TEC.2008.918612>.